Bachelor thesis

Assessing the kinetic accessibility of the hydride transfer of the silica-supported organometallic catalyst

David Ullersma

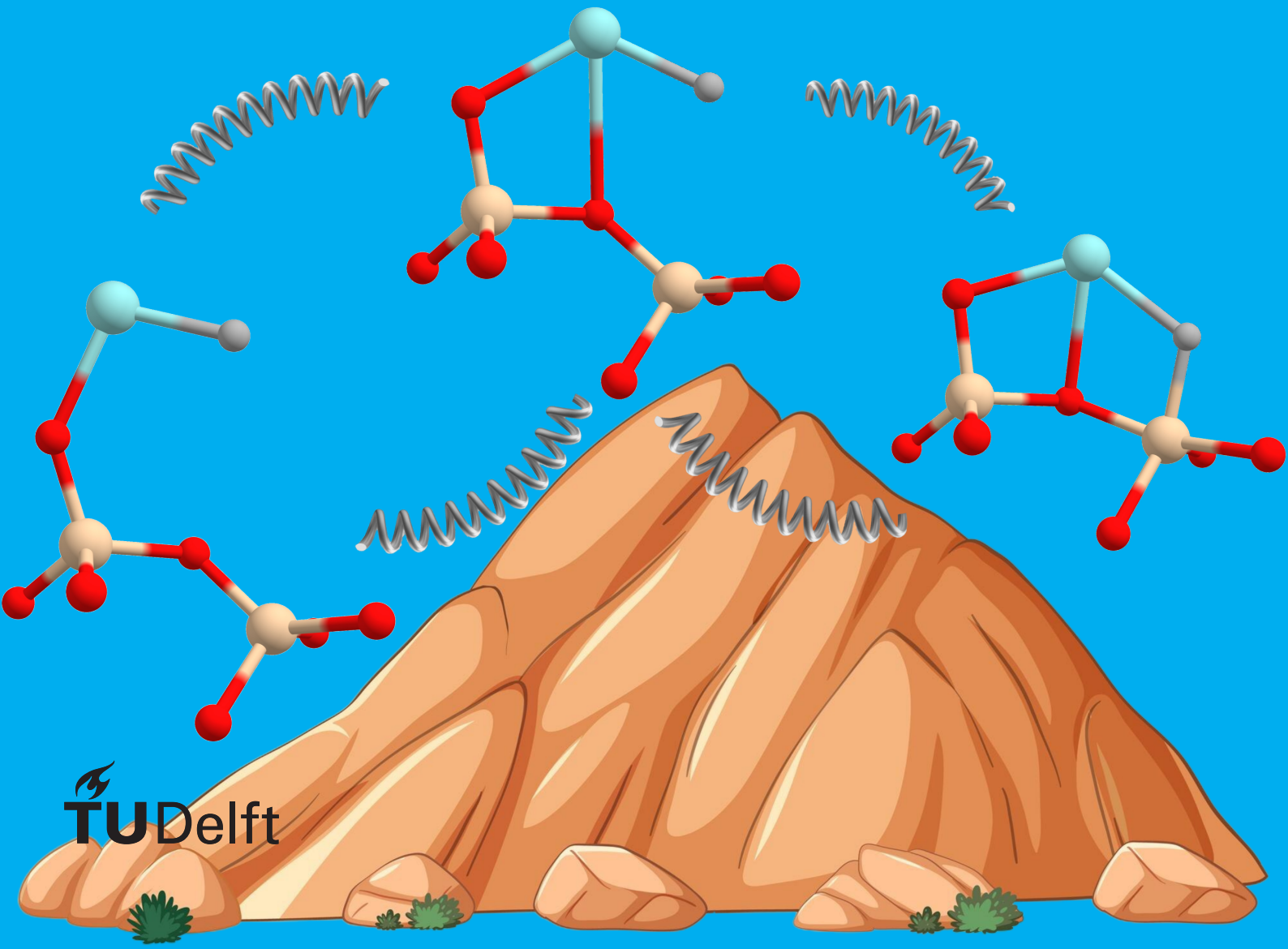

TU Delft

Assessing the kinetic accessibility of the hydride transfer of the silica-supported organometallic catalyst

by

David Ullersma

to obtain the degree of Bachelor of Science
at the Delft University of Technology,
to be defended publicly on Thursday July 4, 2024 at 10:00 AM.

Student number: 5663091
Project duration: April 22, 2024 – July 5, 2024
Thesis committee:

Prof. dr. E. Pidko,	TU Delft, Principle investigator
Dr. A. Kolganov,	TU Delft, Daily supervisor
Dr. J. Meyer,	Leiden University, Second examiner

TU Delft

Contents

1 Abstract **1**

2 Introduction **3**
2.1 Plastic waste . . . 3
2.2 Catalysis . . . 3
2.3 Research background . . . 4
2.4 Research outlook . . . 4
2.5 Structure . . . 5
2.6 list of abbreviations . . . 6

3 Theory **7**
3.1 PES . . . 7
3.2 DFT . . . 7
3.3 Functionals . . . 7
3.4 Basis sets . . . 8
3.5 CP2K and VASP . . . 9
3.6 Dispersion correction . . . 9
3.7 CI-NEB . . . 10
3.8 Vibrational analysis . . . 11

4 Computational details **13**
4.1 CP2K . . . 13
4.2 VASP . . . 13
4.3 Models . . . 13
4.3.1 Comas-vives model . . . 13
4.3.2 Reconstruction . . . 14
4.3.3 Beta-cristobalite . . . 14
4.3.4 In-house model . . . 15
4.4 Grafting . . . 15

5 Results and discussion **17**
5.1 Non-reconstructed amorphous silica surface . . . 19
5.2 Reconstructed amorphous silica surface . . . 19
5.3 Beta-cristobalite . . . 20
5.4 Minimum strain amorphous silica surface . . . 20
5.5 Average strain amorphous silica surface . . . 21
5.6 Maximum strain amorphous silica surface . . . 22
5.7 Effects of surface on kinetic accessibility . . . 22

6 Conclusion **25**
6.1 Conclusion . . . 25
6.2 Further research suggestions . . . 25

A Appendix: additional theory **31**
A.1 Ionic relaxation . . . 31
A.2 IDPP . . . 31
A.3 Geometry optimization with dimer method . . . 32

B Appendix: additional figures and tables **33**
B.1 NEB . . . 33
B.2 Transition states . . . 36
B.3 Tables . . . 42

C Appendix: additional remarks **43**
C.1 Acknowledgements 43
C.2 Use of generative AI 43
C.3 Data management 43
C.3.1 VASP 44
C.3.2 CP2K 44

1

Abstract

A large portion of plastic waste is burned or put into a landfill, which are unsustainable practices. Recycling is a good solution to increase circularity, but currently a significant part of plastic is recycled mechanically. Mechanical recycling reduces the quality of the plastic, consequently plastic can only be recycled a few times before it needs to be discarded. This significant downside can be solved by chemical recycling aided by catalysis. The investigated zirconium catalyst ($^{Bu}Cp_2ZrH-OSi$) is supported on an amorphous silica surface. The ISE group at the TU Delft has developed a configurational space exploration algorithm that has found states of this supported catalyst, which are far more thermodynamically stable compared to a chemical guess. Many stable states are the result of the hydride transfer from Zr to Si. The thermodynamic stability does not only determine if the state can be accessible at the reaction conditions (80°C), the kinetics must also be considered as well. To determine the kinetic accessibility, the hydride transfer activation energies were estimated for various amorphous silica surfaces as well as perfect beta-cristobalite. The Cristobalite and minimum strain silica surface showed relatively high energy reaction barriers (≈96-107 kJ/mol) compared to the higher strain surfaces (≈15-54 kJ/mol). This shows that the reaction barrier is highly dependent on the surface structure. The found barriers show that the configurational space exploration algorithm can find kinetically accessible states at reaction conditions.

2

Introduction

2.1. Plastic waste

Plastics improved consumer goods substantially because it is cheap, though, chemically resistant, a good electrical insulator and versatile [1]. Each year around ~370 MT of plastic is produced, consequently this results in a significant amount of plastic waste, however globally only around 20 % of the plastic waste is being recycled [2]. One reason this percentage is not higher is because the mechanical recycling process is currently expensive and creates lower quality plastic than virgin plastic. The biggest source of waste is plastic packaging. Primarily plastic packaging is made from five main polymers: High Density PolyEthylene (HDPE), Low Density PolyEthylene (LDPE), PolyPropylene (PP) and PolyEthylene Tereftalate (PET)[3, 4].

The lowering in quality due to mechanical recycling is primarily the result of contamination [5]. Despite extensive washing of the plastic waste, contaminates still remain on and in the plastic waste. There are a lot of different contaminates for plastic waste, a few will be discussed. Coating and paints are one type of contaminate, which can be insoluble causing phase separation and thus reducing mechanical properties. Plastics can also be degraded by UV-light which can create structures detrimental to the mechanical properties. Another type of contaminate are in-chain contaminates, meaning unusual chemical groups or atoms attached to the chain such as hydroxyl groups and chloride atoms. Plastic can also contain fillers, colourants and plasticisers to tune the properties of the plastic, which can also lower the quality of the recycled plastic [6, 7].

Because of these flaws chemical recycling solutions have been proposed as a way to improve plastic recycling. One chemical recycling technique uses catalysts to degrade the chemically inert C-C bonds found in polyolefins.

2.2. Catalysis

There are three main types of catalysis: heterogeneous, homogeneous and bio-catalysis. Homogeneous catalysis is well-defined, but it does require separation from the product as they are in the same phase. An advantage of heterogeneous catalysis is that it does not face this problem as the catalyst is in a different phase from the product. However heterogeneous catalysis is less-defined and is usually less selective.

Surface OrganoMetallic Chemistry (SOMC) combines advantages of heterogeneous and homogeneous catalysis, because it uses organometallic complexes grafted on a bulk support material. There are numerous advantages to using SOMC over traditional heterogeneous catalysis. One such advantage is that the organometallic complexes can be designed using the knowledge of coordination chemistry, which is a well-researched field. Another advantage is that all catalytic sites are similar, this increases the specificity and makes the system more well-defined. A third advantage is that interaction between two organometallic complexes is prevented, because of the rigid surface [8]. The catalysis can be designed even further by choosing a support material that can help stabilize reaction intermediaries, thus helping in the catalytic activity of the catalyst. All these advantages have led to improvements in reactions such as alkane metathesis, Ziegler Natta depolymerization and oxidative dehydrogenation

[9, 10]. Specifically relevant for the recycling of PE is Ziegler Natta deplymerization, better known as hydrogenolysis [11]. This reaction depolymerizes polyolefins such as PE.

2.3. Research background

Many different transition metal complexes have been investigated as possible catalysts for hydrogenolysis [12]. One possible candidate for depolymerization at low temperatures of PE is 1,1'-dibutylzirconocene dichloride ($^{Bu}Cp_2ZrCl_2$). After activation of the pre-catalyst, the catalyst ($^{Bu}Cp_2ZrH_2$) can react with a surface hydroxyl group (SiOH) to form the supported complex ($^{Bu}Cp_2ZrH-OSi$) which is used in plastic polymerization and can be used for low temperature (80°C) hydrogenolysis [13, 14].

Hydrogenolysis is the reaction where a C-C bond gets cleaved and hydrogen is added in place. This can be repeated to cleave polymers into smaller hydrocarbons. This reaction is difficult due to the high stability and chemical inertness of the C-C bonds. The mechanistic pathway for hydrogenolysis of polyolefins is not entirely known but the most probable mechanism found can be described by Figure 2.1 [12, 8].

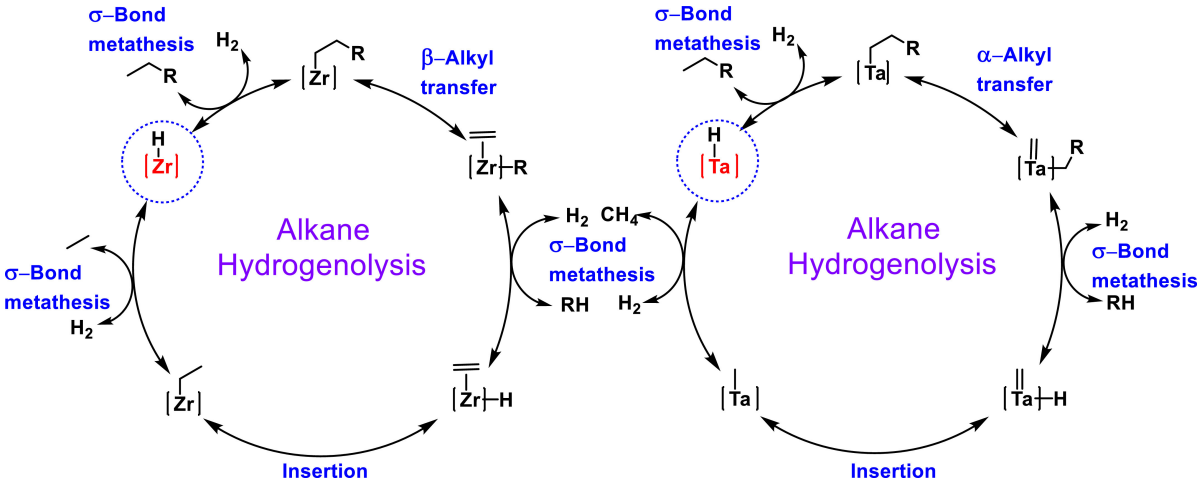

Figure 2.1: A schematic representation of the hydrogenolysis reaction [8]

As mentioned before we consider SOMC in principle to generate identical sites (single site), but in reality it is more complicated. Industry usually uses amorphous materials, therefore amorphous materials must be considered. This complicates the catalytic sites of SOMC even more. In the case of amorphous silica, complications include siloxane rings, strained surface regions and hydroxyl groups [15]. The ISE group of TU Delft has developed a configurational space exploration algorithm to discover the ensemble of states of the amorphous silica-based catalyst based on molecular dynamics and graph theory (Figure 2.2). New thermodynamically stable states of the supported catalyst beyond the initial guess structure have been found by use of this algorithm, but if these states are formed in reality is not only determined by its thermodynamic accessibility but also by the kinetic accessibility. A large portion of stable states show a hydride that has been transferred from Zr to a surface Si atom. These states deactivate the catalyst and are therefore undesirable.

This report aims to investigate the kinetic accessibility of the stable states found by the configurational space exploration algorithm. To accomplish this the rate constants will be calculated with the reaction barrier energies which will be found using computational methods.

2.4. Research outlook

The hydride transfer reaction (Figure 2.3) is the reaction pathway to the thermodynamically stable states so the barrier of this reaction will be investigated. With these results it can be determined if the algorithm can find kinetically accessible states, or it could lay a foundation for its improvement.

This mechanism (Figure 2.3) was examined on amorphous silica surfaces generated by Comas-Vives (2016)[16], beta-cristobalite and amorphous silica surfaces generated by M.P. Klein according to the algorithm described by Nguyen et al. (2023)[17].

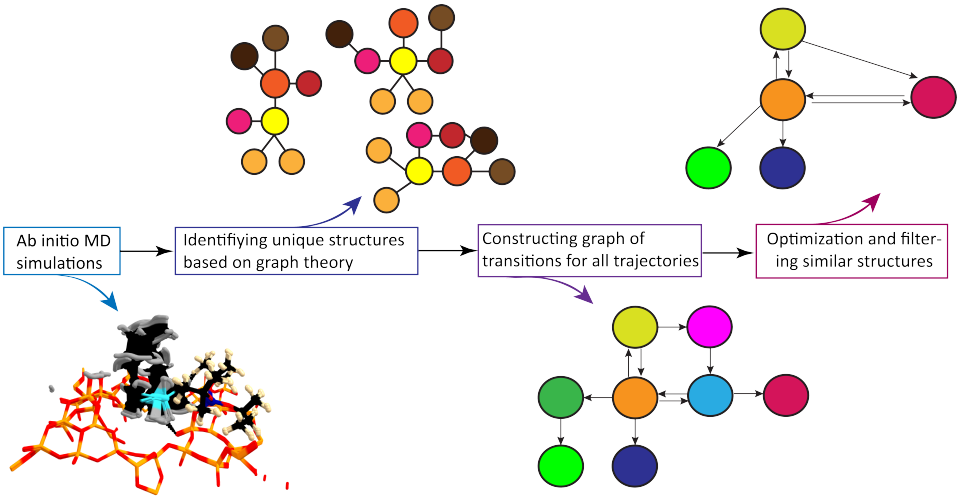

Figure 2.2: Overview of the workflow of the configurational space exploration algorithm developed in ISE

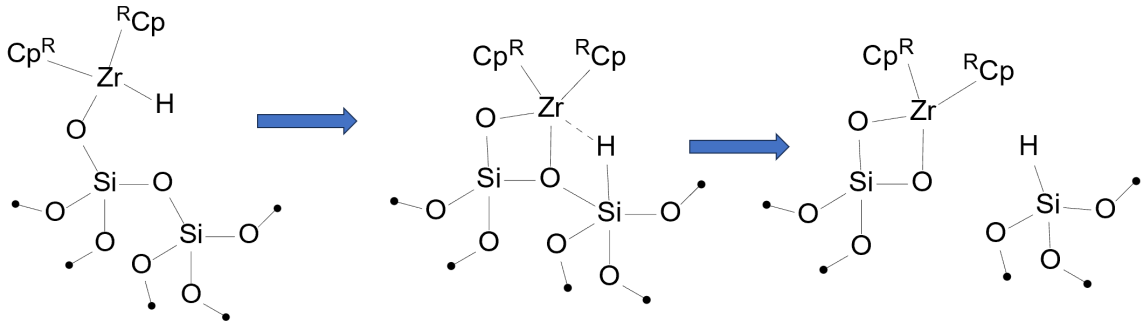

Figure 2.3: The investigated mechanism of hydride transfer from the Zr atom to the surface Si atom.

2.5. Structure

The rest of the report will start by discussing the theory behind the used computational methods. Then the computational details of the methods will be presented. Finally, the results will be discussed and a conclusion will be drawn from the discussed results.

2.6. list of abbreviations

- SOMC: surface organometallic chemistry
- PE: polyethylene
- VASP: Vienna ab inito simulation package
- DFT: density functional theory
- LDA: local density approximation
- GGA: general gradient approximation
- STO: slater type orbital
- GTO: Gaussian type orbital
- PW: plane wave
- PAW: projection augmented wave
- GPW: Gaussian plane wave
- GAPW: Gaussian-augmented plane wave
- PBE: Perdew-Burke-Ernzerhof (functional)
- vdW: van der Waals
- NEB: nudged elastic band
- CI-NEB: climbing image nudged elastic band
- PES: potential energy surface
- MEP: minimum energy path
- TS: transition state
- SP: saddle point
- IDPP: image dependant pair potential
- TS1: transition state between the initial and intermediate state
- TS2: transition state between the intermediate and final state
- IS: inital state
- IntS: Intermediate state
- FS: final state

3

Theory

3.1. PES

An important concept in transition state chemistry is the Potential Energy Surface (PES). The PES describes the potential energy of the system against the coordinates of the system. On this energy surface the stable states of the system can be found as minima. Between these minima the reaction barrier can be found. The transition state of this reaction barrier is characterized by the first-order saddle point on the reaction barrier as can be seen in Figure 3.1.

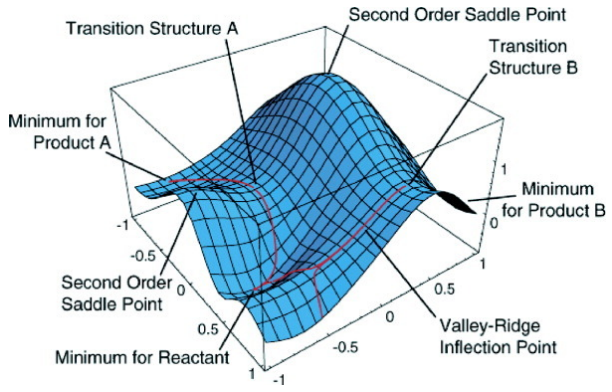

Figure 3.1: A schematic representation of the PES showing minima, transiton states, second order saddle points and a valley-ridge inflection point[18].

3.2. DFT

To simulate the molecules of interest density functional theory (DFT) is used. DFT optimizes the electron density instead of wave functions, as was done before in the Hatree Fock (HF) approach. Kohn and Sham laid the basis of DFT, they postulated that just like the HF approach variational theorem could be used to find the electron density of the system. They also developed the framework to actually find the electron density and divided the energy up in 4 terms: the kinetic energy of the non-interacting electrons, the nuclear-electron interaction, the classical electron-electron repulsion and the exchange-correlation energy. The exchange-correlation includes the correction to the kinetic energy from the interactions between electrons and all non-classical corrections to electron-electron repulsion energy [19, 20].

3.3. Functionals

This exchange-correlation energy is unknown and is approximated with a functional. One group of functionals uses the local density approximation (LDA), this means that the functional can be computed at each point only using the electron density at that point. This approximation was expanded by

including the gradient of the electron density being considered, this is known as the general gradient approximation (GGA)[19]. Further approximations include exact exchange energies and are therefore significantly more computationally expensive. One important concept in computational chemistry is the trade-off between accuracy and the computational cost. This is best described by the Jacob's ladder of Perdew shown in Figure 3.2.

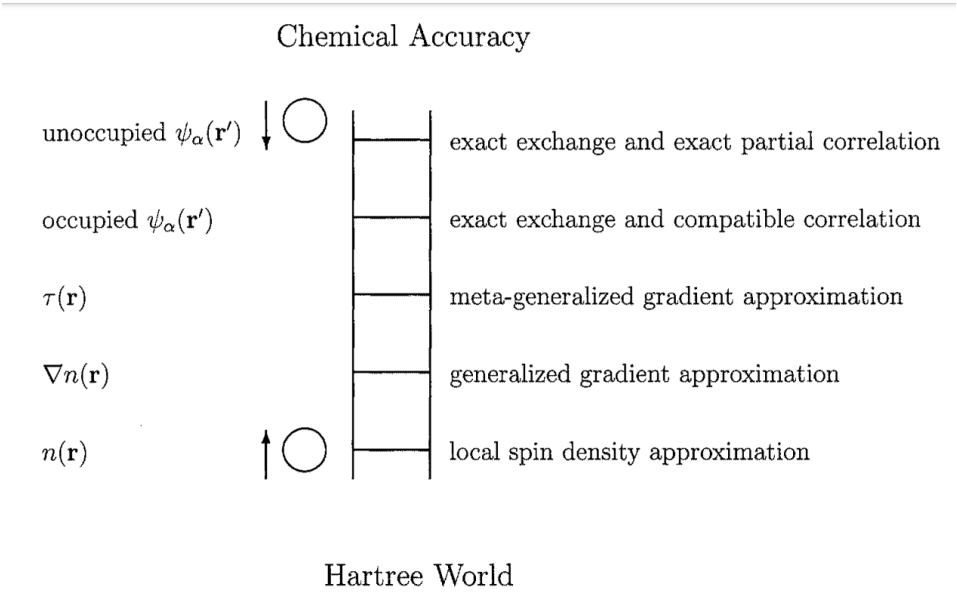

Figure 3.2: The Jacob's ladder of functionals showing the accuracy trade-off [21].

A popular variant of GGA is Perdew-Burke-Ernzerhof functional (PBE) [22]. This functional gives a good balance between accuracy and computational cost and is therefore used in this research.

3.4. Basis sets

A basis set is a collection functions, in computational chemistry these basis functions are used to model the electronic wave function. When only one basis function per orbital is used it is called a minimal basis set, this set is accurate as long as there is no interaction with other orbitals, which in real systems is seldom the case so more basis functions are added that increase the flexibility of the orbitals to change based on their environment. These extra functions are called polarisation functions. In theory more and more functions can be added to approach a complete basis set which describes the electronic wave function without introducing extra error. Instead of trying to approach this complete basis set a more incomplete or smaller basis set is used as the error introduced by basis set incompleteness is usually relatively small compared to other errors. There are three main types of basis functions, namely Slater type orbital (STO), Gaussian type orbital (GTO) and plane wave (PW). The STO basis set has an exponential form (Eq:3.1) and is inspired by the form of hydrogen-like wave functions.

$$f_n^{STO}(r_A) = r_A^l e^{-\zeta r_A} \tag{3.1}$$

Although the STO basis set was a good initial guess as it was based on already solved systems it was computationally expensive and therefore was replaced with the GTO basis set. The quantum mechanical operators are substantially easier to numerically evaluate with Gaussian's. As the name suggests the functions take on a Gaussian form instead of an exponential one. A new variation of the GTO was developed as a single Gaussian function cannot approximate the wave function with enough accuracy. This new basis set uses a linear combination of Gaussian's (Eq: 3.2) and is called the contracted Gaussian orbital (CGTO) basis set. The amount of Gaussian basis functions used per valance orbital is denoted by ζ. For example, a double ζ basis set uses two basis functions for each valance orbital.

$$f_l^{CGTO}(r_A) = r_A^l \sum_i d_i e^{-\alpha_i r_A^2} \tag{3.2}$$

The plane wave basis set has the form: $\phi(\mathbf{r}) = e^{i\mathbf{rk}}$. Where $\mathbf{k}$ is the reciprocal lattice vector. This basis set is most prominently used in periodic systems such as solid state systems as plane waves are inherently periodic. As mentioned before approaching a complete basis set is too computationally expensive and therefore the plane wave basis set is truncated. This is done with a cutoff energy, meaning all plane waves with kinetic energy up to and including this energy are used and the rest are discarded[23, 24].

3.5. CP2K and VASP

Many different methods or approximations have been developed, relevant for this research is the projector augmented wave method (PAW), because it is the basis for the Vienna Ab Inito Simulation Package (VASP) and partly CP2K, the software packages used in this research. CP2K uses a version of this method called the Gaussian-augmented plane wave method (GAPW), while VASP uses the standard PAW formalism.

The PAW method splits the wave function into two parts one for the core electrons and one for the valance electrons. This is because the two regions differ significantly in respect to the wave function. The wave function close to the nucleus oscillates rapidly and is highly localized, while the wave function at the valance electrons is smooth and diffuse. The core region is expensive to accurately describe as the node structure of the core electrons can only be described by a prohibitively large plane wave basis set.

One common method used in combination with PAW to simplify the core wave function is the frozen core approximation. In this approximation the electron densities of the core electrons are precomputed as a free atom. In other words, this approximation removes the influence of external electrons to the core electrons. This approximation can be made because the valance electrons screen the highly localized core electrons.

The main way PAW simplifies the system is by using a special pseudopotential instead of the real potential from the core electrons. A pseudopotential is a means to efficiently represent the influence of the core electrons over the valance electrons by transforming the wave function of the core electrons into one that is more easily computed. Note that the potential is changed in the core region but is matched to the real potential outside the core region. PAW distinguishes itself in defining this pseudopotential in such a way to in the end retain the nodal structure, while still reducing the computational cost [25, 26].

CP2K offers multiple DFT methods, most prominently the Gaussian plane wave method (GPW) and the Gaussian augmented plane wave method (GAPW). GPW uses a contracted Gaussian basis set to describe the wave function and an auxiliary plane wave basis set to describe the electron density. GAPW combines the PAW and GPW methods to get the benefits of both approaches[27].

3.6. Dispersion correction

DFT calculations have struggled to simulate London dispersion forces between molecules and atoms, which leads to inaccuracies. A dispersion correction is used to give accurate dispersion interactions where DFT can not. Similarly to functionals a lot of different dispersion corrections have been developed each having a trade-off between accuracy and computational cost. Dispersion forces also known as van der Waals (vdW) forces are long-range electronic interactions between atoms. These interactions are caused by the charge density change on one atom that causes the formation of a dipole moment that induces a dipole of the second atom. This interaction has a decay of $-1/r^6$. This decay is not reproduced by PBE or similar functionals and this leads to a systematic underestimating the binding strength of these interactions (Figure 3.3). One of the more simple and computationally efficient dispersion corrections is D3(BJ) which is part of the DFT-D dispersion correction family. The computational efficiency and simplicity of DFT-D comes from the fact that DFT-D computes the dispersion energy independently from the Kohn-Sham energy. The total energy can then be defined as the sum of the Kohn-Sham energy and the dispersion energy ($E_{tot} = E_{KS} + E_{disp}$). The dispersion energy is calculated pairwise additive as can be seen in Equation: 3.3.

$$E_{disp} = -\sum_{AB}\sum_{n=6,8,10,..} \frac{C_n^{AB}}{R_{AB}^n} f_{damp,n}(R_{AB}, A, B) \tag{3.3}$$

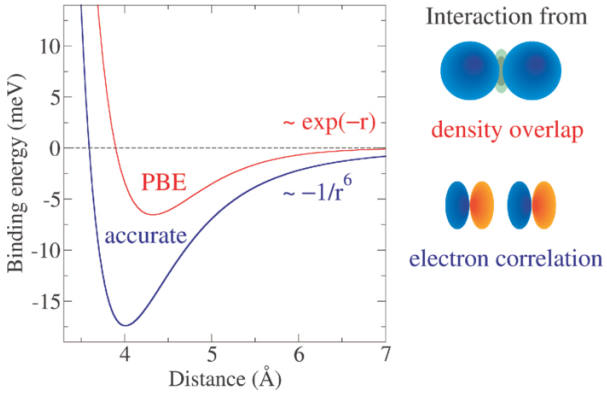

Figure 3.3: The real decay of dispersion forces compared to the forces modeled by PBE [28].

Equation: 3.3 can be split into three parts. The first part is the summation of all pairs of atoms, here denoted as A and B. The second part is the application of the $C_n R^{-n}$-potentials. Where R_{AB}^n is the internuclear distance between atom A and B to the power n. The C_n^{AB} coefficients are specific for each atom pair AB. In theory the summation of the coefficients has no end and therefore must be truncated. Generally DFT-D only uses the C_6 term, but this can be too inaccurate for some applications. D3(BJ) uses the C_6 and C_8 term and truncates the rest. Other more accurate dispersion schemes also include the C_{10} term. There are multiple ways these coefficients are gathered. The easiest and most inaccurate method has static coefficients that are determined beforehand. More sophisticated methods calculate these values based on the environment such as the one used in D3(BJ). The last part is the dampening function. This function is a correction on the $C_n R^{-n}$ potentials which diverge at small distances. The implementation of this dampening function varies between dispersion schemes but in general the function is one for large values of r and the function decreases the energy to zero or a constant value for small values of r. An example of the effect of the dampening function can be seen in Figure: 3.4 [28, 29].

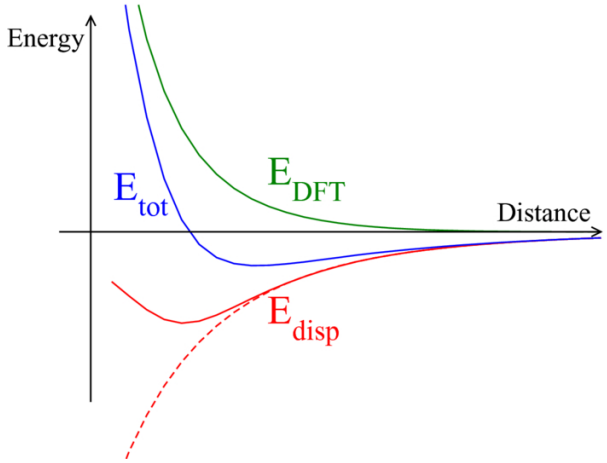

Figure 3.4: The energy contributions to approximate the dispersion the real energy profile. The solid red line indicates the dispersion energy with dampening function and the dotted line what the dispersion energy would be if the dampening function was not applied [28].

3.7. CI-NEB

The Climbing Image Nudged Elastic Band (CI-NEB) method is a relevant computational method for this research as it can be used to find the transition state between two stable states. CI-NEB tries to find the Minimum Energy Path (MEP) on the PES (Figure 3.5). The MEP is defined by being the local minimum energy in the orthogonal directions to the path. The transition state of this MEP is located at the first-order Saddle Point (SP) on the PES. A first-order saddle point is a local minimum in all

directions but one in which it is a maximum.

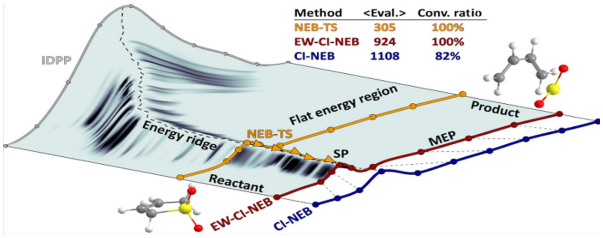

Figure 3.5: A minimum energy path on a potential surface found by NEB methods starting from IDPP generated images[30].

Two methods exist to find the saddle point. The first method only uses an initial state, from this state the PES is climbed to find the SP. This method is called the dimer method and this method uses two variations of the initial structure to climb the PES. The second method is NEB and it uses an initial and final state. The NEB method starts by interpolating structures between the initial and final state, these structures are called images or replicas. The geometry of the interpolated images is then optimized by ionic relaxation. A force described as a harmonic spring is placed between neighboring images that influences the relaxation. This separates the replicas and prevents them from sliding into each other. The springs before and after the real transition state 'push' the replica closest to the real transition state uphill on the PES in the direction of the real transition state and stabilize this replica (Figure 3.6). CI-NEB is a variation on NEB that changes the geometry optimization of the highest energy replica to find the highest energy structure on the MEP instead of the lowest [30, 31].

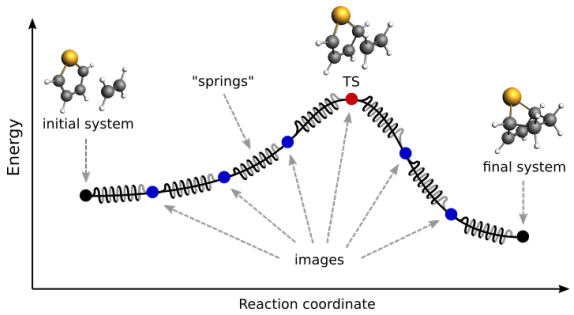

Figure 3.6: A schematic representation of the CI-NEB method [32].

3.8. Vibrational analysis

In vibrational analysis each bond is approximated as a harmonic oscillator. This means the PES is approximated as a parabolic curve following Hooke's law: $U = \frac{1}{2}kx^2$. The second order derivative of the potential U is simply the force constant k: $\frac{d^2U}{dx^2} = k$, these force constants are combined in a matrix called the Hessian. Solving the eigenvalue problem with the hessian results in eigenvalues that are the square of the vibrational frequencies and eigenvectors that describe the normal mode of the corresponding frequency. For transition states all normal modes are positive except one, this 'negative' frequency is called the imaginary frequency. A frequency is imaginary because the square root of its negative eigenvalue from the hessian is an imaginary number. As discussed in the section about NEB, the transition state is located on a first-order saddle point on the PES. This means that the curvature is positive in all directions except one, this direction corresponds with the normal mode with the imaginary frequency [33].

Vibrational analysis in VASP can be done using two methods, namely the finite difference method and the density functional perturbation theory. The finite difference method will be discussed as this is the method used to perform vibrational analysis in this research (see computational details). In general the finite difference method is a way to numerically approximate a derivative. The finite difference method is used in vibrational analysis to calculate the second-order derivatives, which are the force constants k, they are combined in the Hessian and the frequencies and normal modes are then found

with the method described above. To do the finite difference methods three points are required, these

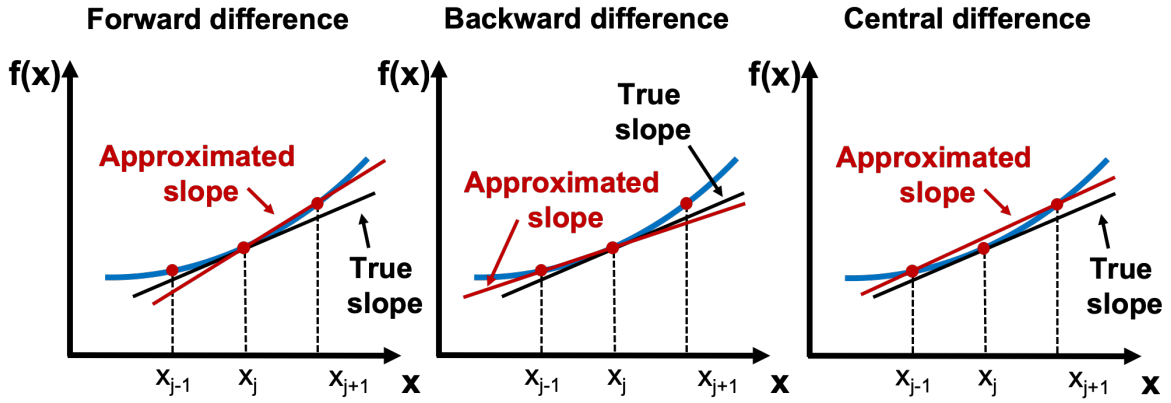

Figure 3.7: Forward, backward and central difference variants of the finite difference method

points are gathered by moving each atom in each Cartesian direction forward and backward by a small amount. The finite difference method can be done in three different ways: the forward difference, backward difference and the central difference (Figure 3.7). VASP uses the central difference method as it is generally more accurate than the forward or backward finite difference method.

4

Computational details

Periodic DFT calculations were performed with CP2K (version 2022.1[27]) and the Vienna Ab inito Simulation Package (VASP 6.4.2[34, 25]). The Perdew-Burke-Emzerhof (PBE) functional was used [22]. The climbing image nudged elastic band (CI-NEB) method was used to determine the transition state structures. CI-NEB was done with 8 replicas, this was increased to 16 when necessary. The highest energy structures found by CI-NEB were optimized again. To confirm the optimized states are in fact transition states vibrational analysis was performed.

4.1. CP2K

The basis set used in CP2K is the Gaussian plane wave basis set (GPW). Light atoms (H,C,O,Si) were described with a double ζ basis set (DZVP-MOLOPT-SR-GTH) while for the heavier zirconium a triple ζ basis set was used (TZV2P-MOLOPT-SR-GTH). The Brillouin zone sampling was restricted to Γ point. The plane wave energy cutoff was set at 450 Ry and the relative cutoff at 30 Ry. CP2K uses 4 convergence criteria: change in geometry (max 3E-3 bohr), RMS change in geometry (max 1.5E-3 bohr), change in gradients (max 4.5E-4 bohr^{-1}hartree) and RMS change in gradients (max 3E-4 bohr^{-1}hartree). The D3(BJ) dispersion correction is used to accurately describe van der Waals forces [29]. The geometry of the highest energy replica (approximate TS) was optimized using the dimer method.

4.2. VASP

The basis set used in VASP is the projector augmented wave function method (PAW) with a plane wave basis set. The Brillouin zone sampling was restricted to Γ point. The plane wave energy cutoff for VASP was set at 400 eV. Convergence of geometry optimization was reached when the force on each atom was below 0.05 eV Å^{-1}. A Gaussian smearing of 0.05 eV is used to simulate band occupation. The D3(BJ) dispersion correction is used to accurately describe van der Waals forces [29]. The geometry of the highest energy replica (approximate TS) was optimized using a quasi-newton algorithm (RMM-DIIS). Vibrational analysis was performed by using the finite difference method in VASP.

4.3. Models

4.3.1. Comas-vives model

Multiple surfaces were considered as mentioned in the introduction. The non-reconstructed surface was generated by Comas-vives(2016) [16]. The method described by Comas-vives(2016) starts with high temperature annealing of a 3 x 3 x 3 cubic β-cristobalite unit cell using classical molecular dynamics. The next step consists of cooling the structure and optimizing it with DFT. In the last step the structure is sliced at the 001 plane at 10 Å and hydroxylating. The final unit cell produced by this method is 21.39 x 21.39 x 34.2 Å. This includes 20 Å of vacuum in the z direction to prevent interactions between itself because of the periodic boundary conditions. Finally for the purposes of this research extra vacuum was added to make the final dimensions 21.39 x 21.39 x 45 Å. Figure 4.1 shows the non-reconstructed amorphous silica surface.

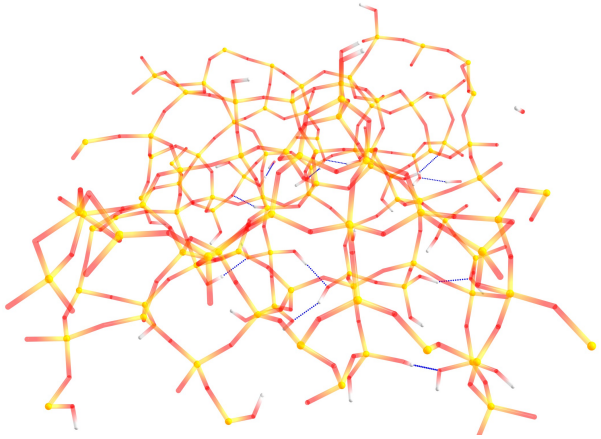

Figure 4.1: The non-reconstructed amorphous silica surface.

4.3.2. Reconstruction

The configurational space algorithm revealed the reconstruction of the surface in the presence of the organometallic core, which lowered the energy of the system significantly. Figure 4.2 shows an example of reconstruction of a silica structure. In this example a strained 2 membered siloxane ring is broken to form a more stable amorphous structure.

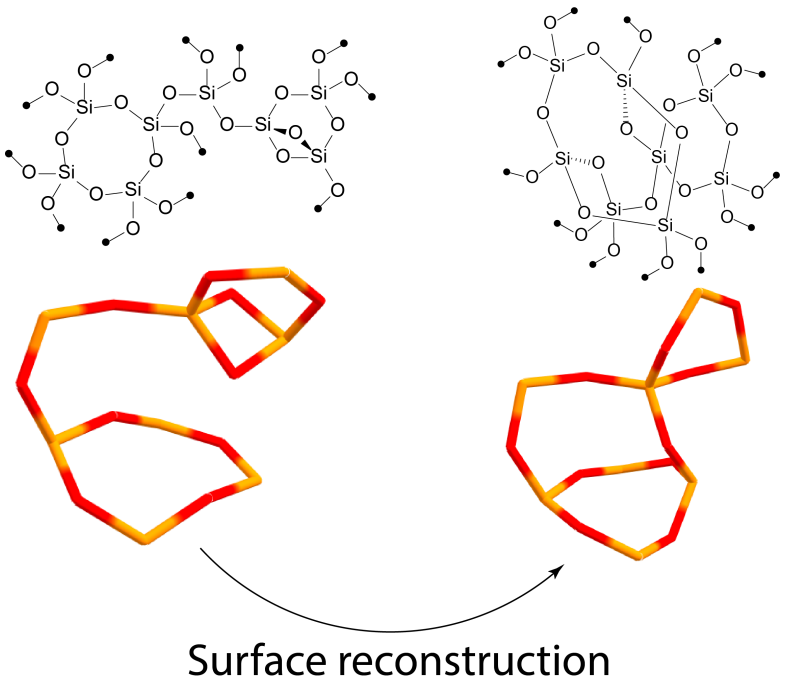

Figure 4.2: An example or surface reconstruction done by the configurational space exploration algorithm.

4.3.3. Beta-cristobalite

The β-cristobalite surface was made by using a β-cristobalite unit cell from the materials project [35] and combining them into a 3 x 3 x 2 structure. Then the top layer of oxygen atoms (001 plane) was removed and the Si atoms at the bottom and the top were replaced with hydrogen atoms to create the final cristobalite surface. The final structure has a unit cell size of 22.3826 x 22.3826 x 45 Å and is characterized by $Si_{108}H_{72}O_{252}$ as the molecular formula.

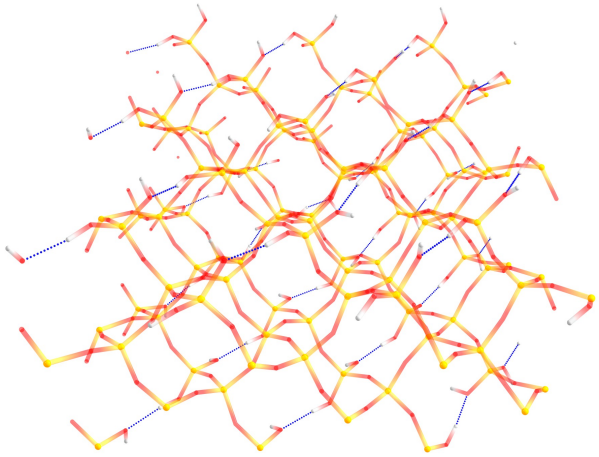

Figure 4.3: The β-cristobalite silica surface.

4.3.4. In-house model

The minimum, average and maximum strain surfaces were generated with the algorithm described in Nuguyen et al. (2023)[17] and in the BEP thesis of M.P. Klein[1]. As described by M. P. Klein in his thesis similarly to Comas-Vives(2016) the generation of the minimum, average and maximum strain surfaces start with high temperature annealing using classical molecular dynamics. Then the surface is cut using a randomly generated stochastic Fourier series to induce roughness of the amorphous silica surface. After cutting the surface is hydroxylated using a genetic algorithm. Sixty structures were generated and of this dataset the surface with the minimum amount of strain, a surface close to the average amount of strain and the surface with the maximum amount of strain were selected. These structures have a unit cell size of 21.5 x 21.5 x 45 Å.

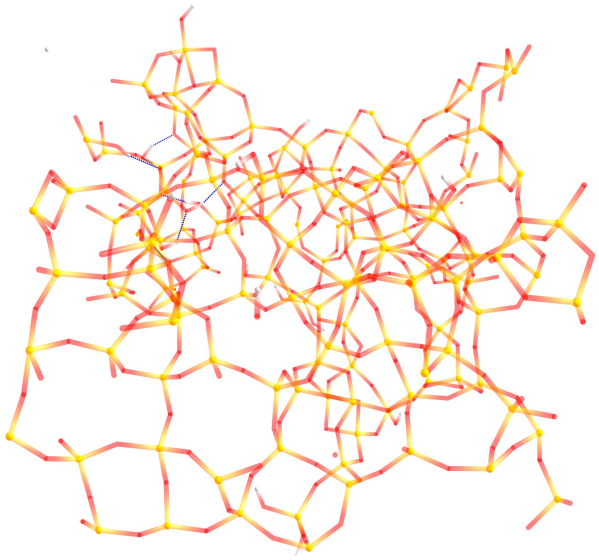

Figure 4.4: The average strain amorphous silica surface.

4.4. Grafting

After these models were made the catalyst ($^{Bu}Cp_2ZrH_2$) is grafted onto the surface. the grafting of the organometallic catalyst is done by reacting with a surface hydroxyl group. In this reaction a hydride and the hydrogen atom from the hydroxyl form H_2 and the oxygen in the hydroxl group is bonded to the zirconium atom.

[1]For more information about the generation of these surfaces read the thesis of M.P. Klein on the ISE storage

5

Results and discussion

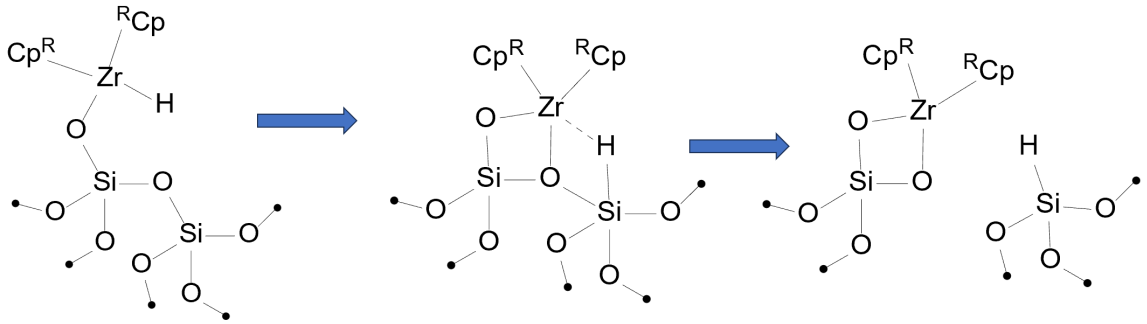

Figure 5.1: The investigated mechanism of hydride transfer from the Zr atom to the surface Si atom.

The investigated structures can be seen in Figure 5.1. The first reaction results in an intermediate in which the hydride is attached to the surface Si atom and still remains in the coordination sphere of the Zr atom. The central oxygen and right silicon are over-coordinated. This is resolved by the second reaction in which this oxygen and the zirconium move away from the right silicon. The results will show if the configurational algorithm developed by ISE can find kinetically accessible states. This algorithm can be implemented in the workflow to find new catalysts for important applications such as plastic recycling.

Initially CP2K was used to run geometry optimizations, NEB calculations and vibrational analysis. After finding finding multiple approximate transition states with the method described in computational details, vibrational analysis was performed. Instead of one expected imaginary frequency, 7 were found with energies up to approximately 400 cm^{-1}. These results were unsatisfying, so it was decided to switch to using VASP. When NEB was done with VASP on the same structures similar NEB energy profiles were generated for the non-reconstructed surface, but for the reconstructed surface higher energy replicas were observed (Figure 5.2). This justifies the switch to VASP as CP2K had missed the reaction barrier and transition state of first reaction of the reconstructed amorphous silica surface and found two significantly lower energy barriers on the second reaction of the reconstructed surface.

Finding the TS for the studied systems was not trivial because of a few reasons. The first one is size, the total system is 400-500 atoms meaning a very high dimensional PES. This has the effect that the system has many local minima near the initial and final states and resulted in the NEB finding better starting and final structures by changing the surface to better suit the catalyst. This relaxation problem was exacerbated by the two connected NEB calculations. This meant that the first NEB could show a normal profile where the first and second to last replicas are higher than the initial and final structures respectively. However the second NEB one could show more stable structures on the first replica. This

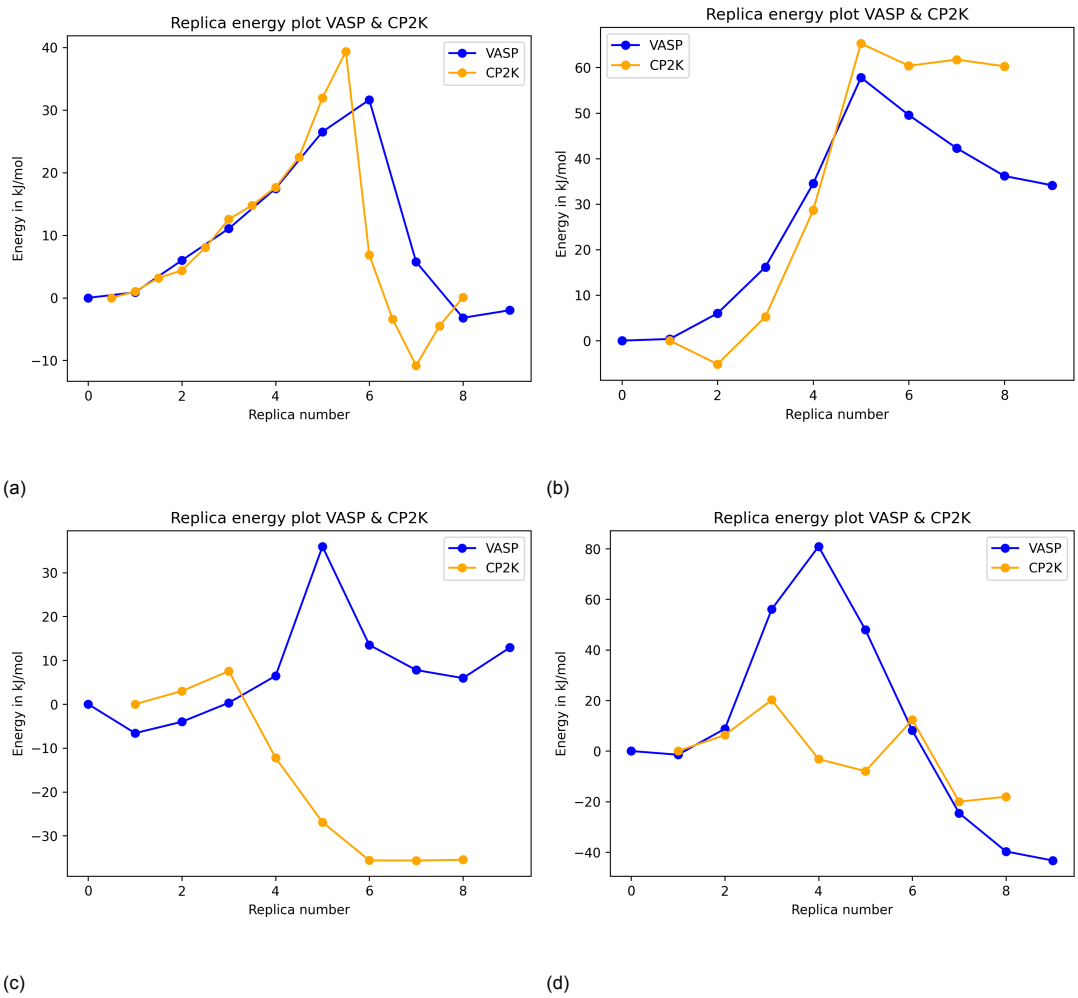

Figure 5.2: The NEB energies of the (a,b) non-reconstructed and (c,d) reconstructed silica surface calculated by CP2K (orange) and VASP (blue). (a,c) from the initial state to the intermediate state. (b,d) from the intermediate state to the final state.

more stable structure could then be used in a new iteration of the first NEB calculation and the second NEB calculation. Despite the earlier success of the first NEB it could find more stable structures yet again. Secondly, the change in structure between the states is rather large, this can result in the NEB jumping the barrier. Thirdly vibrational analysis was done to confirm the transition states, but because of the large number of moving atoms in the reaction mechanism this proved to be difficult and in the end too computationally expensive. To reach this conclusion frequency analysis was performed on an increasing number of atoms. This showed the second approximate transition state of the catalyst on the reconstructed surface to be a real transition state, but only when a large number of atoms was included. This collection of atoms consisted of the Zr atom, the two ^{Bu}Cp rings with the butyl groups, the SiO4 tetrahedral which connected to the Zr atom and all neighboring or connected Si tetrahedrals including the tetrahedral of the Si atom that received the hydride. Another reason for the large computational cost is that vibrational analysis without symmetry is an inherently computationally expensive task. Finally all replicas are connected with forces or 'springs' as described in the theory section, this can result in higher energy structures than the approximate TS, so it may be necessary to further optimize the approximate TS. Because of these difficulties and constraints, it is probable approximate transition states have been found instead of real ones. Although inaccuracies have been introduced by NEB all high energy replicas that could be transition states have been optimized afterwards thereby minimizing the possible inaccuracies.

5.1. Non-reconstructed amorphous silica surface

The non-reconstructed surface was generated by Comas-Vives(2016) [16]. This surface was used in the configurational space exploration algorithm to find the reconstructed surface. Figure 5.3 shows the

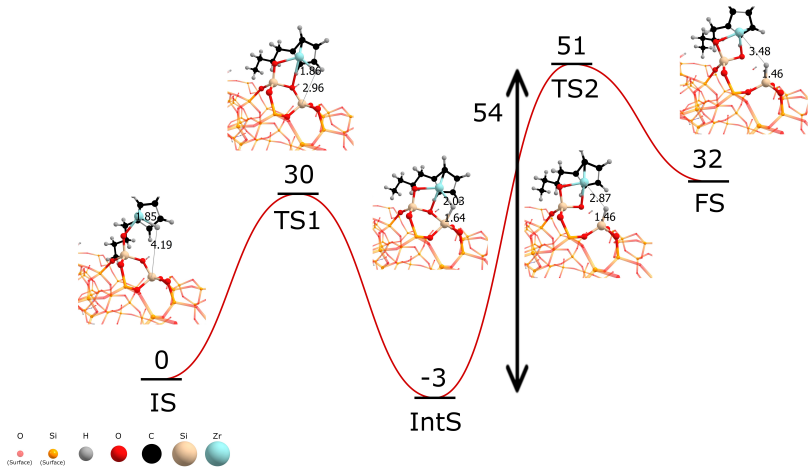

Figure 5.3: The reaction energy diagram of the reaction mechanism on the **non-reconstructed** amorphous silica surface. Energies of each state are given in kJ/mol. As shown in the legend the visual representation of the structure uses grey for hydrogen, black for carbon, red for oxygen, beige for silicon in the active site, orange for silicon in the surface, cyan for zirconium. The active site is highlighted by the use of larger spheres to represent the atoms. The structures of the initial, intermediate, final and transition states are shown with Zr-H and Si-H distances (Å), for visual clarity the front ^{Bu}Cp ring has been removed.

found transition states and its energy in kJ/mol. The first transition state (TS1) is 30 kJ/mol higher than the initial state (IS) which is set as reference point at zero. The intermediate state (IntS) is found to be 3 kJ/mol lower in energy than the reference IS. The second transition state (TS2) is 51 kJ/mol higher than the IS. The second reaction barrier is 54(=51- -3) kJ/mol as this is the energy difference between the IntS (-3 kJ/mol) and the TS2. The final state (FS) is 32 kJ/mol higher than the IS. The second reaction shows the highest energy barrier and therefore the second reaction is considered to be the rate limiting step.

5.2. Reconstructed amorphous silica surface

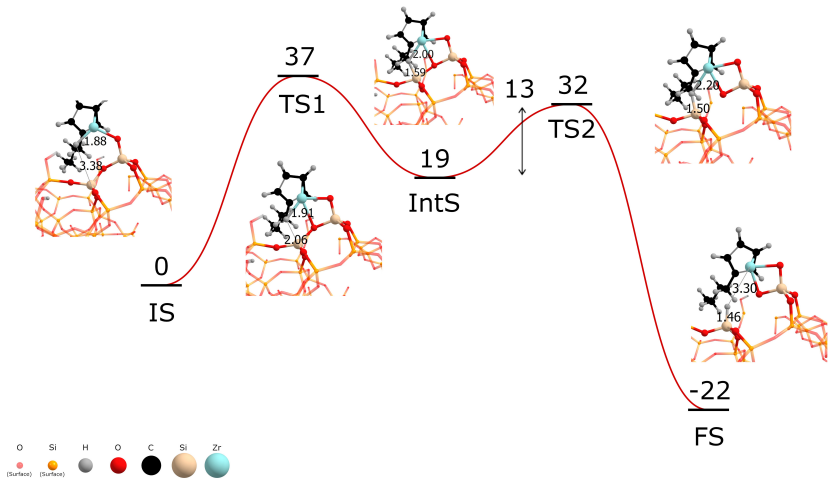

Figure 5.4: The reaction energy diagram of the reaction mechanism on the **reconstructed** amorphous silica surface. Energies of each state are given in kJ/mol. As shown in the legend the visual representation of the structure uses grey for hydrogen, black for carbon, red for oxygen, beige for silicon in the active site, orange for silicon in the surface, cyan for zirconium. The active site is highlighted by the use of larger spheres to represent the atoms. The structures of the initial, intermediate, final and transition states are shown with Zr-H and Si-H distances (Å), for visual clarity the front ^{Bu}Cp ring has been removed.

Figure 5.4 shows the found transition states and its energy in kJ/mol. The first transition state (TS1) is 37 kJ/mol higher than the initial state (IS). The intermediate state (IntS) is found to be 19 kJ/mol higher in energy than the reference IS. The second transition state (TS2) is 32 kJ/mol higher than the IS. The second reaction barrier is 13(=32-19) kJ/mol as this is the energy difference between the TS (32 kJ/mol) and the IntS (19 kJ/mol). The FS is found to be 22 kJ/mol lower than the IS. The primary difference between the non-reconstructed and the reconstructed silica surface is the second reaction barrier energy. Because of reconstruction this barrier has decreased from 54 kJ/mol to 13 kJ/mol. This drop in the reaction barrier can partly be explained by the the energy of the IntS which has increased from -3 kJ/mol to 19 kJ/mol and the FS which has decreased from 32 kJ/mol to -22 kJ/mol. Qualitatively a possible explanation for the decrease in barrier can be that the reconstructed surface has more room or it is less energetically unfavorable for the SiO_3Zr fragment move away from the hydride compared to the non-reconstructed surface.

5.3. Beta-cristobalite

β-cristobalite was investigated as it is crystalline in contrast to the other amorphous silica surfaces. Figure 5.5 shows the found transition states and its energy in kJ/mol. The first transition state (TS1) is

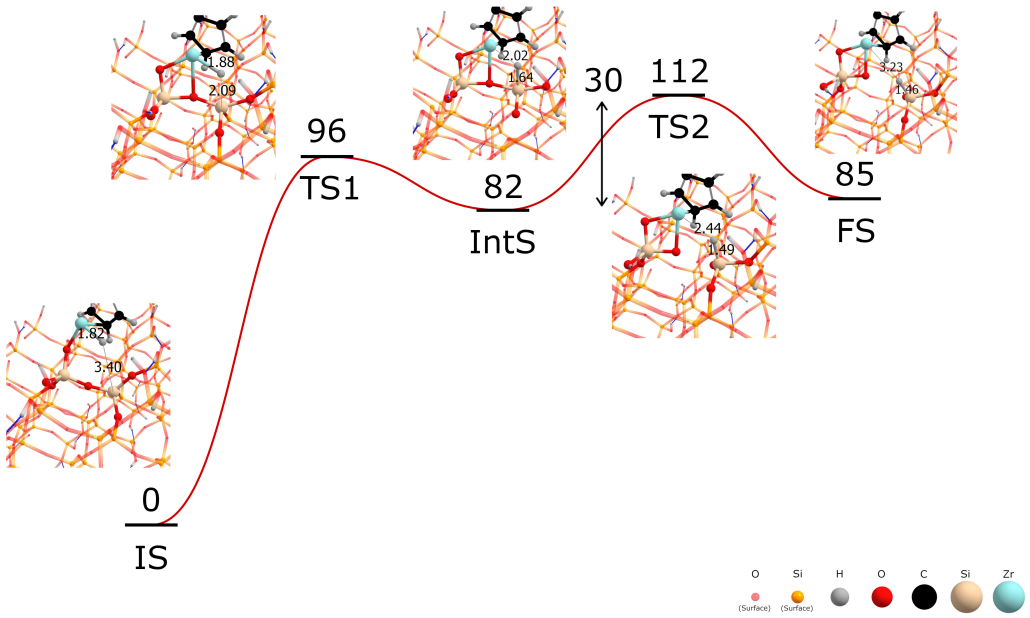

Figure 5.5: The reaction energy diagram of the reaction mechanism on the **cristobalite** silica surface. Energies of each state are given in kJ/mol. As shown in the legend the visual representation of the structure uses grey for hydrogen, black for carbon, red for oxygen, beige for silicon in the active site, orange for silicon in the surface, cyan for zirconium. The active site is highlighted by the use of larger spheres to represent the atoms. The structures of the initial, intermediate, final and transition states are shown with Zr-H and Si-H distances (Å), for visual clarity the front ^{Bu}Cp ring has been removed.

96 kJ/mol higher than the initial state (IS). The intermediate state (IntS) is found to be 82 kJ/mol higher in energy than the reference IS. The second transition state (TS2) is 112 kJ/mol higher than the IS. The second reaction barrier is 30(=112-82) kJ/mol as this is the energy difference between the TS2(112 kJ/mol) and the IntS (82 kJ/mol). The FS is found to be 85 kJ/mol higher than the IS. As expected the energies on the perfect cristobalite are comparatively high because of the introduction of the strained ring between the silicon, oxygen and zirconium while on a perfect crystalline surface without strain.

5.4. Minimum strain amorphous silica surface

As demonstrated by the work of Mas Klein the model of Comas-vives was too strained. Mas Klein looked into generating more realistic amorphous silica surfaces. From this dataset of surfaces a minimum, average and maximum strain surface was selected to be investigated. Figure 5.6 shows the found transition states and its energy in kJ/mol. The first transition state (TS1) is 17 kJ/mol higher than the initial state (IS). The intermediate state (IntS) is found to be 15 kJ/mol higher in energy than the

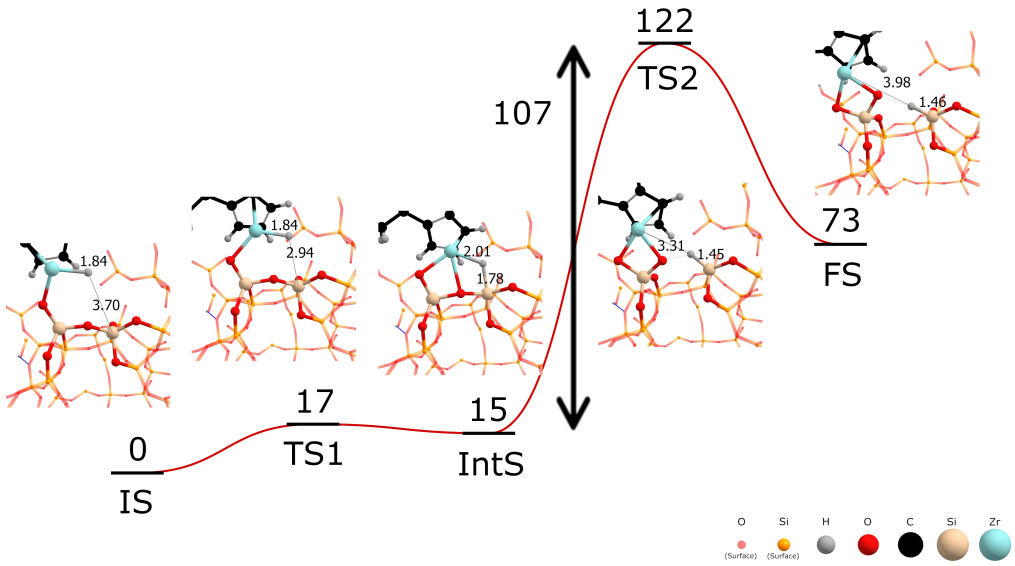

Figure 5.6: The reaction energy diagram of the reaction mechanism on the **minimum strain** amorphous silica surface. Energies of each state are given in kJ/mol. As shown in the legend the visual representation of the structure uses grey for hydrogen, black for carbon, red for oxygen, beige for silicon in the active site, orange for silicon in the surface, cyan for zirconium. The active site is highlighted by the use of larger spheres to represent the atoms. The structures of the initial, intermediate, final and transition states are shown with Zr-H and Si-H distances (Å), for visual clarity the front ^{Bu}Cp ring has been removed.

reference IS. The second transition state (TS2) is 122 kJ/mol higher than the IS. The second reaction barrier is 107(=122-15) kJ/mol as this is the energy difference between the TS2 (122 kJ/mol) and the IntS (15 kJ/mol). The FS is found to be 22 kJ/mol lower than the IS. The rate limiting step is the second reaction as it shows the highest energy barrier, a possible explanation could be the inability of the SiO_3H fragment to move due to local strain as generally this fragment moves in combination with the SiO_3Zr requiring both to move less. Because the inability of the SiO_3H to move the SiO_3Zr fragment needs to move more thereby increasing the energy of the transition and final state.

5.5. Average strain amorphous silica surface

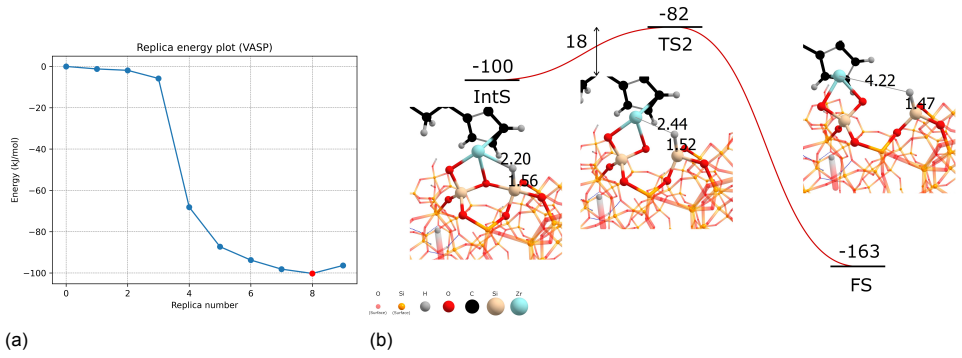

Figure 5.7: (a) the NEB energy profile and (b) The reaction energy diagram of the reaction mechanism on the **average strain** amorphous silica surface. Energies of each state are given in kJ/mol. The connecting point between (a) and (b) is highlighted in red. As shown in the legend the visual representation of the structure uses grey for hydrogen, black for carbon, red for oxygen, beige for silicon in the active site, orange for silicon in the surface, cyan for zirconium. The active site is highlighted by the use of larger spheres to represent the atoms. The structures of the intermediate, final and second transition state are shown with Zr-H and Si-H distances (Å), for visual clarity the front ^{Bu}Cp ring has been removed.

Figure 5.7 shows the NEB energy profile (Sub-figure:5.7a) of the first reaction barrier and the re-

action energy diagram (Sub-figure:5.7b) of the second reaction barrier. The NEB energy profile does not show any clear TS. It is probable that due to the small size of this barrier the NEB has jumped over the barrier. Replica 8 of the first NEB shows a lower energy and is therefore considered to be the IntS (-100 kJ/mol). This point is the start of the reaction energy diagram. The transition state of the second reaction is found to be 18 kJ/mol higher than the IntS. The final state energy is 163 kJ/mol lower than the IS. A possible reason for the exceptional stability of the FS could be the Si linking the SiO_3H and SiO_3Zr fragments combined with minimal local strain. This linking Si could allow the two fragments to move apart without or with comparatively little extra strain introduced in the surface compared to other surfaces.

5.6. Maximum strain amorphous silica surface

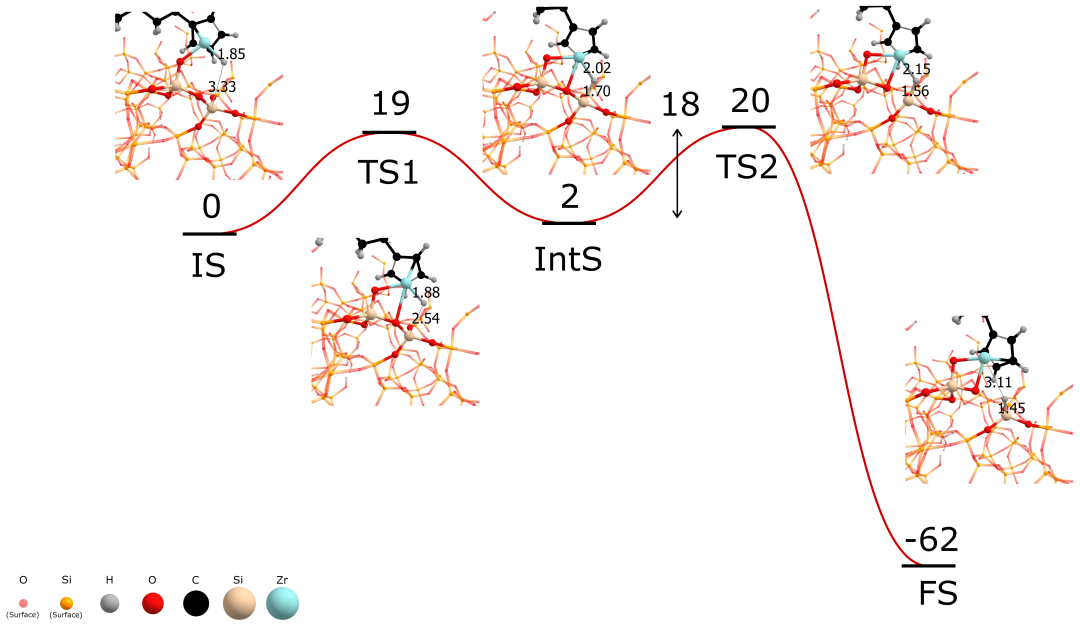

Figure 5.8: The reaction energy diagram of the reaction mechanism on a **maximum strain** amorphous silica surface. Energies of each state are given in kJ/mol. As shown in the legend the visual representation of the structure uses grey for hydrogen, black for carbon, red for oxygen, beige for silicon in the active site, orange for silicon in the surface, cyan for zirconium. The active site is highlighted by the use of larger spheres to represent the atoms. The structures are shown with Zr-H and Si-H distances (Å), for visual clarity the front ^{Bu}Cp ring has been removed.

Figure 5.8 shows the found transition states and its corresponding energy in kJ/mol. The first transition state (TS1) is 19 kJ/mol higher than the initial state (IS) and the barrier is therefore the same. The intermediate state (IntS) is 2 kJ/mol higher than the IS. The next barrier is 18 kJ/mol as this is the difference between the energy of the TS2 (20 kJ/mol) and the IntS (2 kJ/mol). The FS has a significantly lower energy than the IS of -62 kJ/mol.

5.7. Effects of surface on kinetic accessibility

Low strain structures such as the crystalline cristobalite and the low strain amorphous silica surface show relatively high energy final structures and high reaction barriers (≈96-107 kJ/mol). Interesting to note is that the cristobalite has a high reaction barrier for the first reaction barrier while the minimum strain surface has the high reaction barrier on the second reaction barrier. the higher strain surfaces (high strain, non-reconstructed, reconstructed) show lower reaction barriers (≈15-54 kJ/mol). The low and non-existent barriers of the average strain surface suggest there is an optimal amount of strain to reduce the reaction barrier. However, it could be that the average strain reaction barrier is an outlier and that is reaction barrier stems from a unique structure of the active site on the average strain surface. This would mean the general relation between the reaction barrier energy and strain could be negative. As described in the Bell-Evans-Polanyi principle it can be noted that the stability of the final structure is

correlated with the height of the reaction barrier. This correlation seems to be consisted across lower energy barriers but the sample size is rather small to make definitive claims about this relation.

$$k = Ae^{-\frac{E_a}{RT}} \tag{5.1}$$

With the reaction barrier energies the rate constants can be found using the Arrhenius equation (Eq:5.1). A standard pre-exponential factor can be calculated by $A = \frac{k_b T}{h}$, where k_b is the Boltzmann constant, T is the temperature and h is the Planck constant as described by transition state theory [36, 37]. The operating temperature of the catalyst is 80 °C or 353 K with this the standard pre-exponential is 7.36E12. Table 5.1 shows all the highest reaction barriers with their corresponding rate constant.

If kinetic accessibility is defined as $k >> 1$ all states are kinetically accessible except the β-cristobalite

Surface	E_a kJ/mol	k s^{-1}
Non-reconstructed	54	7.5E4
Reconstructed	36	3.5E7
β-cristobalite	96	4.6E-2
minimum strain	107	1.1E-3
average strain	18	1.6E10
maximum strain	19	1.1E10

Table 5.1: The highest reaction barrier energies with their respective rate constant.

IntS, FS (by extension) and the FS of the minimum strain surface. This gives a positive outlook on the ability of the configurational search algorithm to find kinetically accessible states as the β-cristobalite is not an amorphous silica surface and the minimum strain surface is an extreme.

In broader context, the accessibility of the states where the hydride on the Zr atom has transferred to the surface Si atom removes catalysts from the catalytic cycle. This means that the data shows that the investigated mechanism negatively impacts the catalytic performance of the zirconium catalyst.

6

Conclusion

6.1. Conclusion

In this work the reaction barriers of hydride transfer of the Zr atom to the Si surface atom were assessed. It was discovered that CI-NEB with CP2K was unsuitable for the investigated system and that VASP was a good alternative. The cristobalite and the minimum strain silica surfaces show that stable surface structures have relatively high energy barriers (≈96-107 kJ/mol). Higher strain silica surfaces (non-reconstructed, reconstructed, maximum strain) show lower barriers of 15 kJ/mol to 59 kJ/mol. No reaction barrier has been found for the first reaction of the average strain surface, while the second reaction barrier is found to be 18 kJ/mol. In general it can be stated that the energy of the reaction barrier of the investigated reaction barrier is highly dependent on the silica surface as each surface has significantly different barrier energies. Based on the data it can be concluded that the configurational space exploration algorithm is able to find kinetically accessible states at the operating temperature of the catalyst (80°C) as the non-reconstructed, reconstructed, average and maximum strain surfaces show reaction barriers that lead to sufficiently high rate constants ($k >> 1$).

6.2. Further research suggestions

Further research could look into local strain of the sites to more accurately determine the effect of the strain on the kinetic accessibly. This could include finding the transition states on the same surface at different locations. Another unanswered question in this report is the Bell-Evans-Polanyi correlation, this correlation could be investigated further and may provided more insight into the difference between the barriers. The average strain surface could be investigated more thoroughly by using an auto-NEB algorithm [38]. This algorithm updates the number of replicas to narrow down to the TS and this may be able to find the low energy TS. As described in results and discussion the NEB repeatedly found more stable structures by relaxing the surface, further research could investigate this phenomenon and try to develop a method to better investigate these surfaces. The workflow for finding transition states could be improved by using python libraries that make it easier to combine multiple steps such as running jobs, formatting the data and analysing the data. Examples of libraries include Atomic Simulation Environment (ASE), PYCP2K and PyRetis.

Bibliography

[1] Sara Ronca. “Polyethylene”. In: *Brydson’s Plastics Materials: Eighth Edition* (Jan. 2017), pp. 247–278. DOI: 10.1016/B978-0-323-35824-8.00010-4.

[2] Kishor V. Khopade, Samir H. Chikkali, and Nagaraju Barsu. “Metal-catalyzed plastic depolymerization”. In: *Cell Reports Physical Science* 4 (5 May 2023). ISSN: 26663864. DOI: 10.1016/j.xcrp.2023.101341.

[3] Kim Ragaert, Laurens Delva, and Kevin Van Geem. “Mechanical and chemical recycling of solid plastic waste”. In: *Waste Management* 69 (Nov. 2017), pp. 24–58. ISSN: 0956-053X. DOI: 10.1016/J.WASMAN.2017.07.044.

[4] Dusan Jeremic. “Polyethylene”. In: Wiley-VCH Verlag GmbH & Co. KGaA, Aug. 2014, pp. 1–42. DOI: 10.1002/14356007.a21_487.pub3.

[5] S. M. Al-Salem, P. Lettieri, and J. Baeyens. *Recycling and recovery routes of plastic solid waste (PSW): A review*. Oct. 2009. DOI: 10.1016/j.wasman.2009.06.004.

[6] M. K. Eriksen et al. “Contamination in plastic recycling: Influence of metals on the quality of reprocessed plastic”. In: *Waste Management* 79 (Sept. 2018), pp. 595–606. ISSN: 0956-053X. DOI: 10.1016/J.WASMAN.2018.08.007.

[7] Alexander A. Kolganov, A. Sreenithya, and Evgeny A. Pidko. “Homogeneous Catalysis in Plastic Waste Upcycling: A DFT Study on the Role of Imperfections in Polymer Chains”. In: *ACS Catalysis* 13 (20 Oct. 2023), pp. 13310–13318. ISSN: 21555435. DOI: 10.1021/acscatal.3c03269.

[8] Manoja K. Samantaray et al. “Surface organometallic chemistry: A sustainable approach in modern catalysis”. In: *Journal of Organometallic Chemistry* 945 (July 2021), p. 121864. ISSN: 0022-328X. DOI: 10.1016/J.JORGANCHEM.2021.121864.

[9] Jérémie D.A. Pelletier and Jean Marie Basset. “Catalysis by Design: Well-Defined Single-Site Heterogeneous Catalysts”. In: *Accounts of Chemical Research* 49 (4 Apr. 2016), pp. 664–677. ISSN: 15204898. DOI: 10.1021/acs.accounts.5b00518.

[10] Samir Barman et al. “Single-Site VOx Moieties Generated on Silica by Surface Organometallic Chemistry: A Way to Enhance the Catalytic Activity in the Oxidative Dehydrogenation of Propane”. In: *ACS Catalysis* 6 (9 Sept. 2016), pp. 5908–5921. ISSN: 21555435. DOI: 10.1021/acscatal.6b01263.

[11] Manoja K. Samantaray et al. “Surface organometallic chemistry in heterogeneous catalysis”. In: *Chemical Society Reviews* 47 (22 Nov. 2018), pp. 8403–8437. ISSN: 14604744. DOI: 10.1039/c8cs00356d.

[12] Abdulrahman Musa et al. *Review on Catalytic Depolymerization of Polyolefin Waste by Hydrogenolysis: State-of-the-Art and Outlook*. Feb. 2024. DOI: 10.1021/acs.energyfuels.3c04109.

[13] Damien B. Culver et al. “Active Sites in a Heterogeneous Organometallic Catalyst for the Polymerization of Ethylene”. In: *ACS Central Science* 7 (7 July 2021), pp. 1225–1231. ISSN: 23747951. DOI: 10.1021/acscentsci.1c00466.

[14] Felicia D. Cannavacciuolo et al. “A High-Throughput Approach to Repurposing Olefin Polymerization Catalysts for Polymer Upcycling”. In: *Angewandte Chemie - International Edition* 61 (23 June 2022). ISSN: 15213773. DOI: 10.1002/anie.202202258.

[15] Bryan R. Goldsmith et al. “Beyond Ordered Materials: Understanding Catalytic Sites on Amorphous Solids”. In: *ACS Catalysis* 7 (11 Nov. 2017), pp. 7543–7557. ISSN: 21555435. DOI: 10.1021/acscatal.7b01767.

[16] Aleix Comas-Vives. “Amorphous SiO2 surface models: Energetics of the dehydroxylation process, strain, ab initio atomistic thermodynamics and IR spectroscopic signatures”. In: *Physical Chemistry Chemical Physics* 18 (10 2016), pp. 7475–7482. ISSN: 14639076. DOI: 10.1039/c6cp00602g.

[17] Nuong P. Nguyen and Brian B. Laird. “Generation of Amorphous Silica Surfaces with Controlled Roughness”. In: *Journal of Physical Chemistry A* 127 (46 Nov. 2023), pp. 9831–9841. ISSN: 15205215. DOI: 10.1021/acs.jpca.3c04955.

[18] H. Bernhard Schlegel. “Exploring potential energy surfaces for chemical reactions: An overview of some practical methods”. In: *Journal of Computational Chemistry* 24 (12 Sept. 2003), pp. 1514–1527. ISSN: 01928651. DOI: 10.1002/jcc.10231.

[19] Christopher J Cramer. *Essentials of Computational Chemistry Theories and Models Second Edition*. ISBN: 0-470-09182-7.

[20] W Kohn and L J Sham. “PHYSICAL REVIEW Self-Consistent Equations Including Exchange and Correlation Effects*”. In: ().

[21] John P. Perdew. “Jacob’s ladder of density functional approximations for the exchange-correlation energy”. In: AIP Publishing, Feb. 2003, pp. 1–20. DOI: 10.1063/1.1390175.

[22] John P Perdew, Kieron Burke, and Matthias Ernzerhof. *Generalized Gradient Approximation Made Simple*. 1996.

[23] Eva Perlt. *Lecture Notes in Chemistry 107 Basis Sets in Computational Chemistry*. URL: http://www.springer.com/series/632.

[24] Markus Bursch et al. “Best-Practice DFT Protocols for Basic Molecular Computational Chemistry**”. In: (2022). DOI: 10.26434/chemrxiv-2022-n304h. URL: https://doi.org/10.26434/chemrxiv-2022-n304h.

[25] G. Kresse and D. Joubert. “From ultrasoft pseudopotentials to the projector augmented-wave method”. In: *Phys. Rev. B* 59 (3 Jan. 1999), pp. 1758–1775. DOI: 10.1103/PhysRevB.59.1758. URL: https://link.aps.org/doi/10.1103/PhysRevB.59.1758.

[26] *Projector-augmented-wave formalism*. Oct. 2023. URL: https://www.vasp.at/wiki/index.php/Projector-augmented-wave_formalism.

[27] Thomas D. Kühne et al. *CP2K: An electronic structure and molecular dynamics software package -Quickstep: Efficient and accurate electronic structure calculations*. May 2020. DOI: 10.1063/5.0007045.

[28] Jií Klimeš and Angelos Michaelides. “Perspective: Advances and challenges in treating van der Waals dispersion forces in density functional theory”. In: *Journal of Chemical Physics* 137 (12 Sept. 2012). ISSN: 00219606. DOI: 10.1063/1.4754130.

[29] Heiner Schröder, Anne Creon, and Tobias Schwabe. “Reformulation of the D3(Becke-Johnson) Dispersion Correction without Resorting to Higher than C6 Dispersion Coefficients”. In: *Journal of Chemical Theory and Computation* 11 (7 May 2015), pp. 3163–3170. ISSN: 15499626. DOI: 10.1021/acs.jctc.5b00400.

[30] Vilhjálmur Ásgeirsson et al. “Nudged Elastic Band Method for Molecular Reactions Using Energy-Weighted Springs Combined with Eigenvector following”. In: *Journal of Chemical Theory and Computation* 17 (8 Aug. 2021), pp. 4929–4945. ISSN: 15499626. DOI: 10.1021/acs.jctc.1c00462.

[31] Henry C. Herbol, James Stevenson, and Paulette Clancy. “Computational Implementation of Nudged Elastic Band, Rigid Rotation, and Corresponding Force Optimization”. In: *Journal of Chemical Theory and Computation* 13 (7 July 2017), pp. 3250–3259. ISSN: 15499626. DOI: 10.1021/acs.jctc.7b00360.

[32] Software for Chemistry and Materials. *Nudged Elastic Band (NEB)*. URL: https://www.scm.com/doc/AMS/Tasks/NEB.html.

[33] Jack Simons. *ADVANCED THEORETICAL CHEMISTRY*. URL: https://chem.libretexts.org/Bookshelves/Physical_and_Theoretical_Chemistry_Textbook_Maps/Advanced_Theoretical_Chemistry_(Simons).

[34] G Kresse and J Furthmü. *Efficient iterative schemes for ab initio total-energy calculations using a plane-wave basis set*. 1996.

[35] Kristin Persson. *Materials Data on SiO2 (SG:227) by Materials Project*. An optional note. July 2014. DOI: 10.17188/1281939.

[36] Patrick Fleming. *PHYSICAL CHEMISTRY*. URL: https://chem.libretexts.org/Bookshelves/Physical_and_Theoretical_Chemistry_Textbook_Maps/Physical_Chemistry_(Fleming)/11%3A_Chemical_Kinetics_I/11.11%3A_Transition_State_Theory.

[37] Golshani. *6.2.3.6: The Arrhenius Law-Pre-exponential Factors*. URL: https://chem.libretexts.org/@go/page/1448.

[38] Esben L. Kolsbjerg, Michael N. Groves, and Bjørk Hammer. “An automated nudged elastic band method”. In: *Journal of Chemical Physics* 145 (9 Sept. 2016). ISSN: 00219606. DOI: 10.1063/1.4961868.

[39] Søren Smidstrup et al. “Improved initial guess for minimum energy path calculations”. In: *Journal of Chemical Physics* 140 (21 June 2014). ISSN: 00219606. DOI: 10.1063/1.4878664.

[40] Graeme Henkelman and Hannes Jónsson. “A dimer method for finding saddle points on high dimensional potential surfaces using only first derivatives”. In: *Journal of Chemical Physics* 111 (15 Oct. 1999), pp. 7010–7022. ISSN: 00219606. DOI: 10.1063/1.480097.

[41] Penghao Xiao, Qiliang Wu, and Graeme Henkelman. “Basin constrained k-dimer method for saddle point finding”. In: *Journal of Chemical Physics* 141 (16 Oct. 2014). ISSN: 10897690. DOI: 10.1063/1.4898664.

A

Appendix: additional theory

A.1. Ionic relaxation

Ionic relaxation or also known as geometry optimization is generally done in CP2K and VASP with a quasi-newton algorithm implemented with the direct inversion of the iterative subspace (DIIS) method. The quasi-newton algorithm is a collection of computational methods to search for local maxima, minima and zeroes.

A.2. IDPP

A standard way to interpolate the images is linear Cartesian interpolation. Linear Cartesian interpolation is linear interpolation on the three Cartesian coordinates x, y and z. Cartesian interpolation is describes in Equation: A.1.

$$r_{L,i}^{\kappa} = r_i^{\alpha} + \kappa(r_i^{\beta} - r_i^{\alpha})/p \tag{A.1}$$

Where r_i is the coordinates of atom i. The symbol p is the index of the final state counted by starting at the initial state as 0. κ is the index of the interpolated image and thus runs from 1 to $1-p$. α denotes the initial state and β denotes the final state. This type of interpolation with NEB can go wrong, because they can produce high energy structures that could cause issues when optimizing the structure. This problem can be solved by using the Image-Dependant Pair Potential (IDPP) method. This method tries to interpolate the pairwise distances between atoms (Equation: A.2)

$$d_{ij}^{\kappa} = d_{ij}^{\alpha} + \kappa(d_{ij}^{\beta} - d_{ij}^{\alpha})/p \tag{A.2}$$

Where d_{ij}^{κ} is the distance between atom i and j at image index κ. d_{ij} is calculated as $d_{ij} = \sqrt{\sum_{\sigma}(r_{i,\sigma} - r_{j,\sigma})^2}$ with $\sigma = x, y, z$. There are more atom pairs ($N(N-1)/2$) than atomic degrees of freedom($3N-6$) so generally it is not possible to have the calculated d_{ij}^{κ} for each pair. To solve this problem a objective function is defined as described in Equation: A.3

$$S_{\kappa}^{IDPP}(r) = \sum_{i}^{N}\sum_{j>i}^{N} w(d_{ij})\left(d_{ij}^{\kappa} - \sqrt{\sum_{\sigma}(r_{i,\sigma} - r_{j,\sigma})^2}\right)^2 \tag{A.3}$$

Where $w(d_{ij})$ is a weight function used to discourage small distances. Small distance must be discouraged because they are unrealistic high energy structures that can increase the amount of iterations it takes for NEB to converge. A way of looking at this objective function is as the effective energy surface, so NEB can be used on this surface to find optimal starting images [39]. A good comparison and description of the difference between linear Cartesian and IDPP interpolation can be seen in Figure A.1

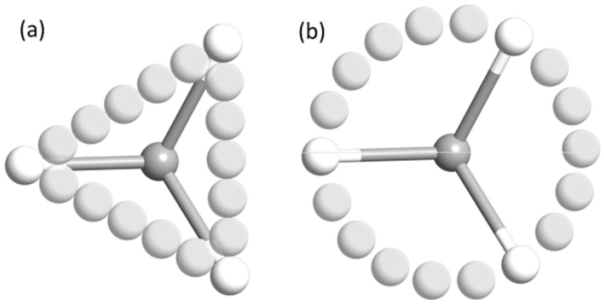

Figure A.1: the images generated by rotation of a methyl group of ethane of (a) linear Cartesian interpolation (b) IDPP interpolation [39]

A.3. Geometry optimization with dimer method

When the highest energy NEB replica is found, its geometry can be optimized using dimer method. The DIMER method tries to find the nearby SP by moving uphill on the PES. While the replica is moving uphill the replica is rotated so to find the lowest curvature [40, 41].

B

Appendix: additional figures and tables

B.1. NEB

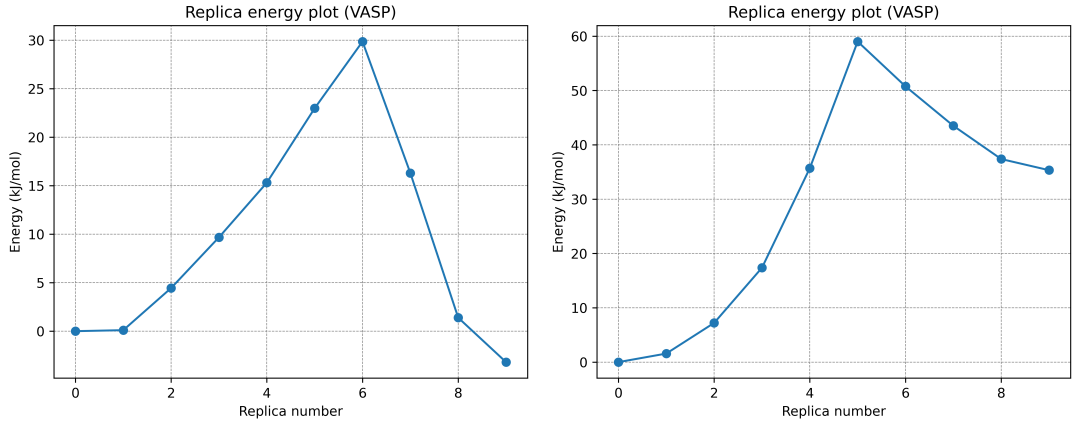

(a) (b)

Figure B.1: The NEB energies of the **non-reconstructed** silica surface. (a) from the initial state to the intermediate state. (b) from the intermediate state to the final state.

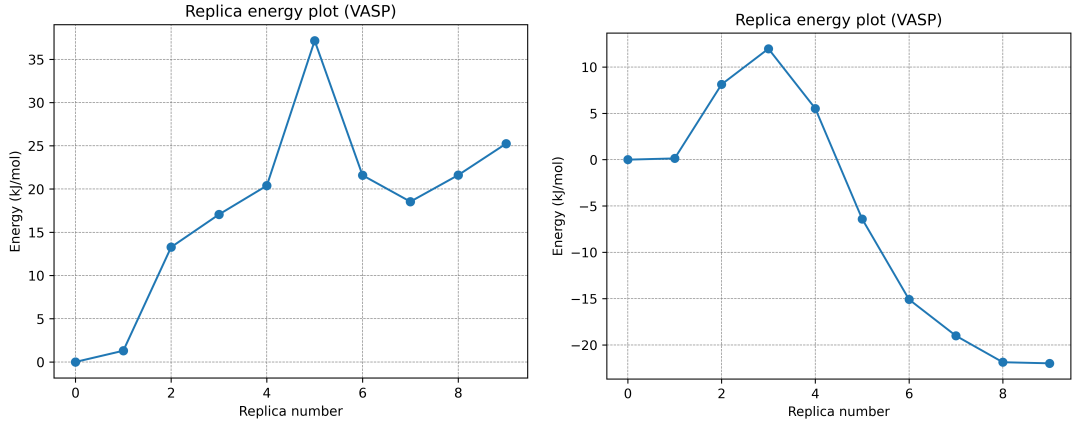

(a) (b)

Figure B.2: The NEB energies of the **reconstructed** amorphous silica surface. (a) from the initial state to the intermediate state. (b) from the intermediate state to the final state.

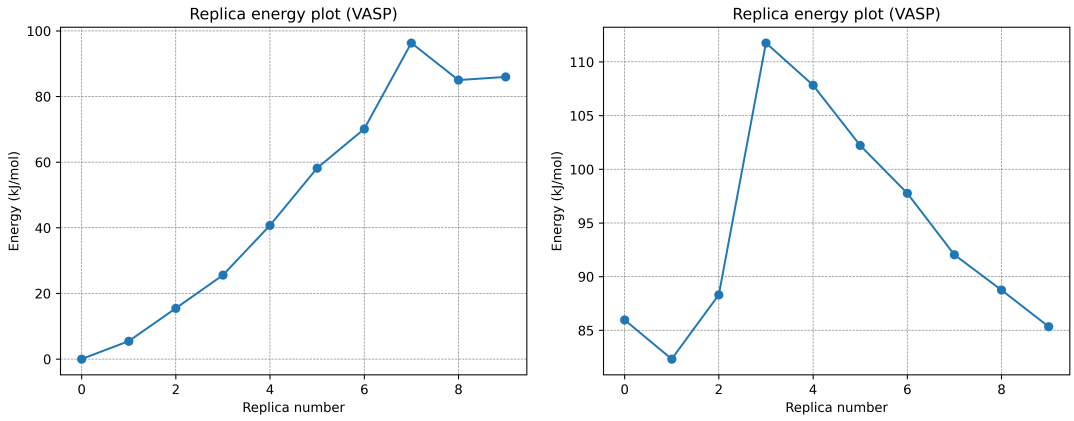

(a) (b)

Figure B.3: The NEB energies of **cristobalite** silica surface. (a) from the initial state to the intermediate state. (b) from the intermediate state to the final state.

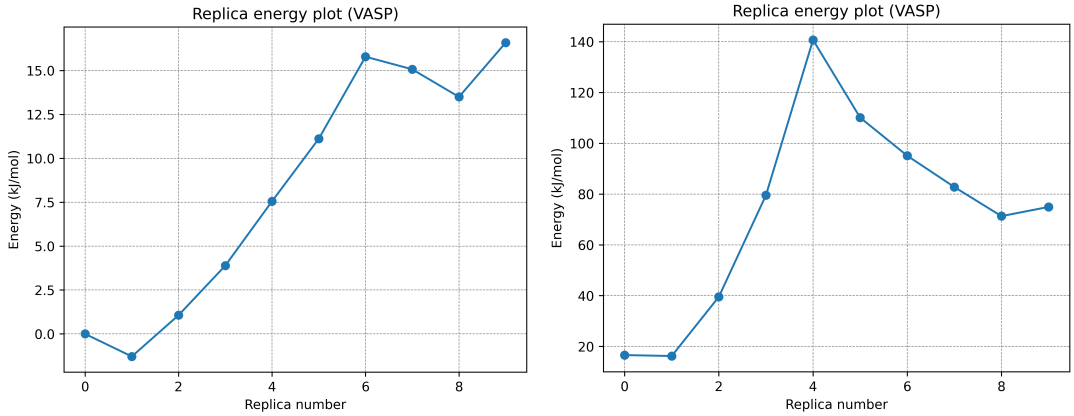

(a) (b)

Figure B.4: The NEB energies of the amorphous silica surface with **minimal strain**. (a) from the initial state to the intermediate state. (b) from the intermediate state to the final state.

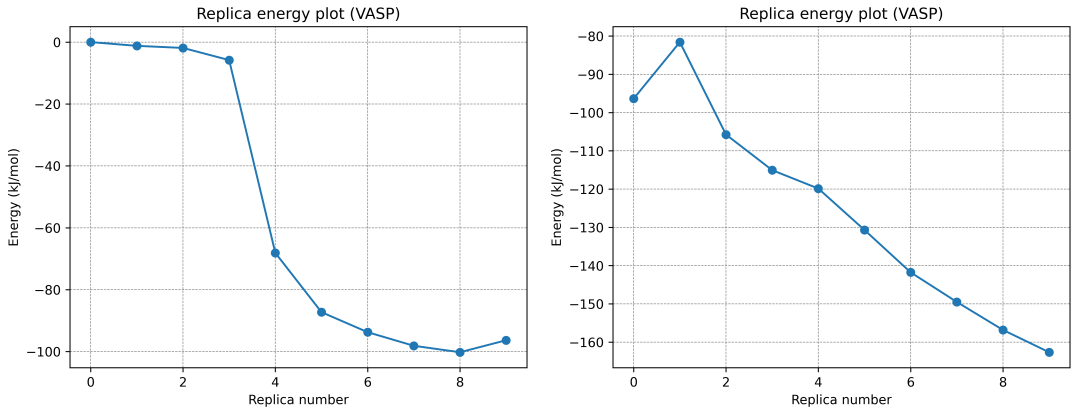

(a) (b)

Figure B.5: The NEB energies of the amorphous silica surface with **average strain**. (a) from the initial state to the intermediate state. (b) from the intermediate state to the final state.

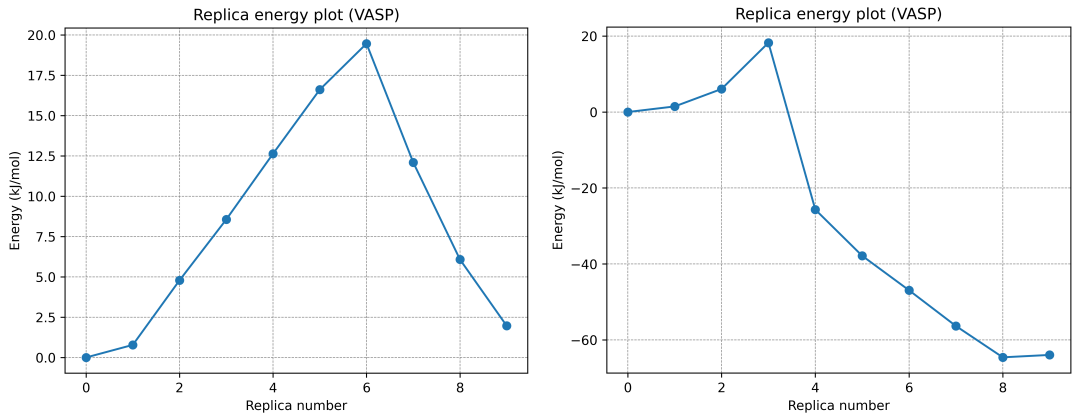

(a) (b)

Figure B.6: The NEB energies of the amorphous silica surface with **maximum strain**. (a) from the initial state to the intermediate state. (b) from the intermediate state to the final state.

B.2. Transition states

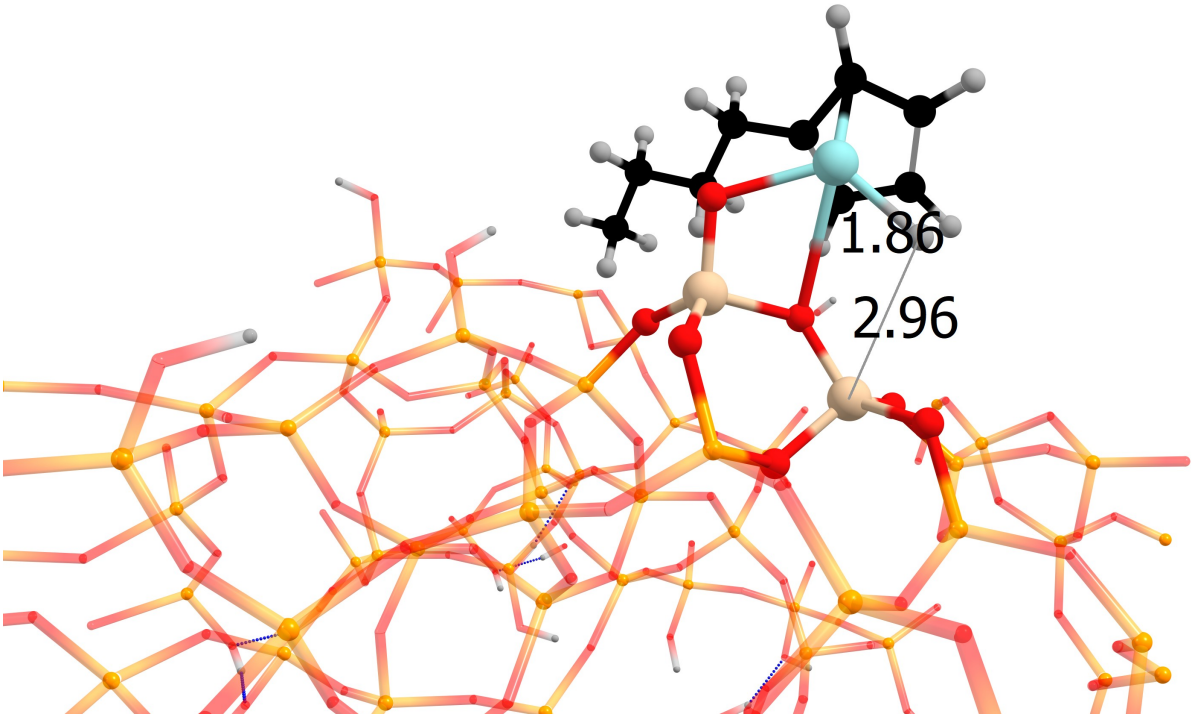

(a) TS1

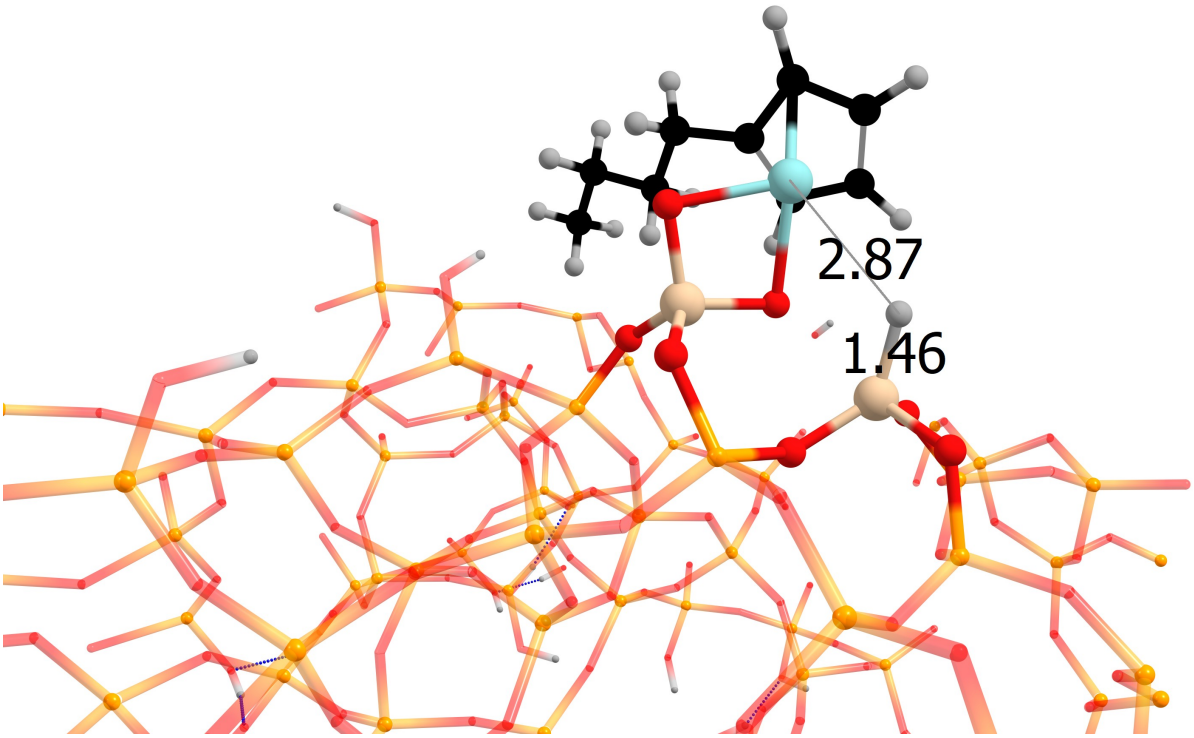

(b) TS2

Figure B.7: The optimized approximate transition states on a **non-reconstructed** amorphous silica surface. (a) the TS between the IS and IntS (b) the TS between the IntS and FS. The visual representation of the structure uses grey for hydrogen, black for carbon, red for oxygen, beige for silicon in the active site, orange for silicon in the surface, cyan for zirconium. The active site is highlighted by the use of larger spheres to represent the atoms. The Zr-H and Si-H distances are shown in Å. For visual clarity the front ^{Bu}Cp ring has been removed.

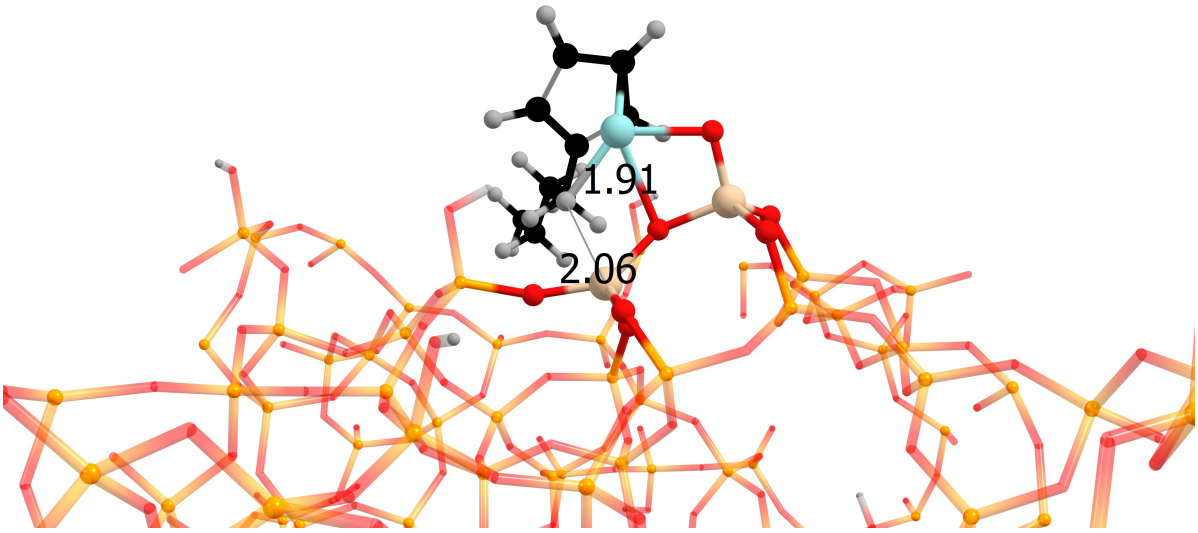

(a) TS1

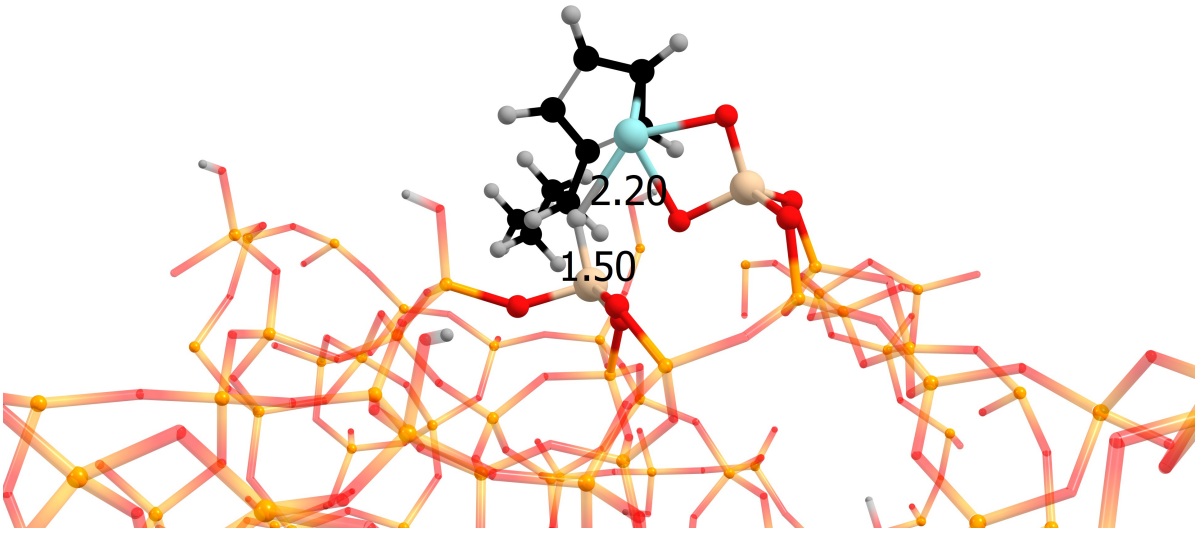

(b) TS2

Figure B.8: The optimized approximate transition states on a **reconstructed** amorphous silica surface. (a) the TS between the IS and IntS (b) the TS between the IntS and FS. The visual representation of the structure uses grey for hydrogen, black for carbon, red for oxygen, beige for silicon in the active site, orange for silicon in the surface, cyan for zirconium. The active site is highlighted by the use of larger spheres to represent the atoms. The Zr-H and Si-H distances are shown in Å. For visual clarity the front ^{Bu}Cp ring has been removed.

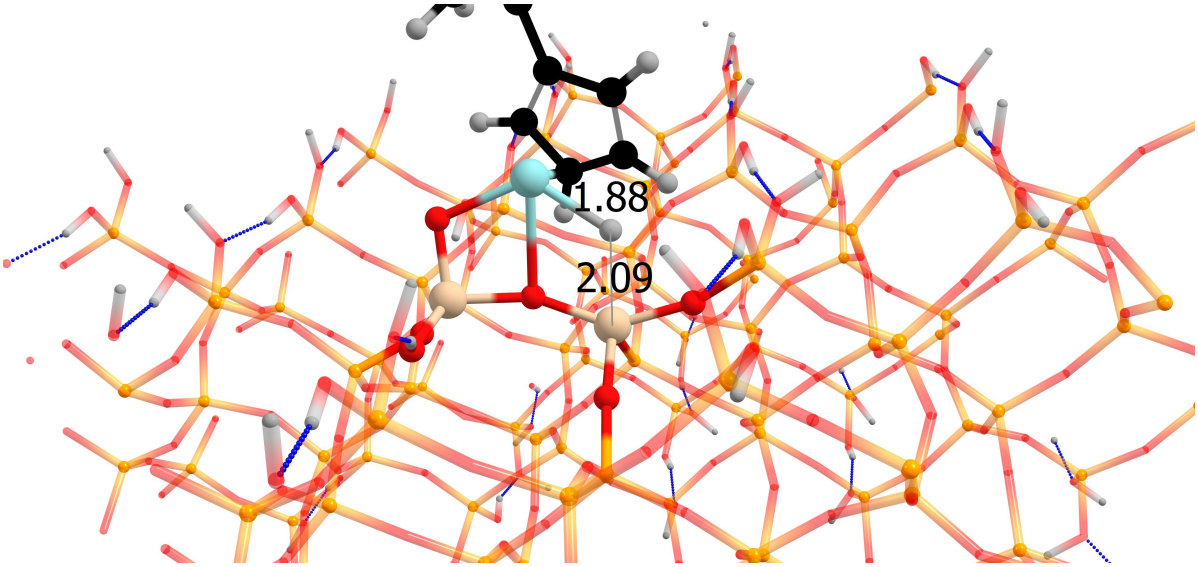

(a) TS1

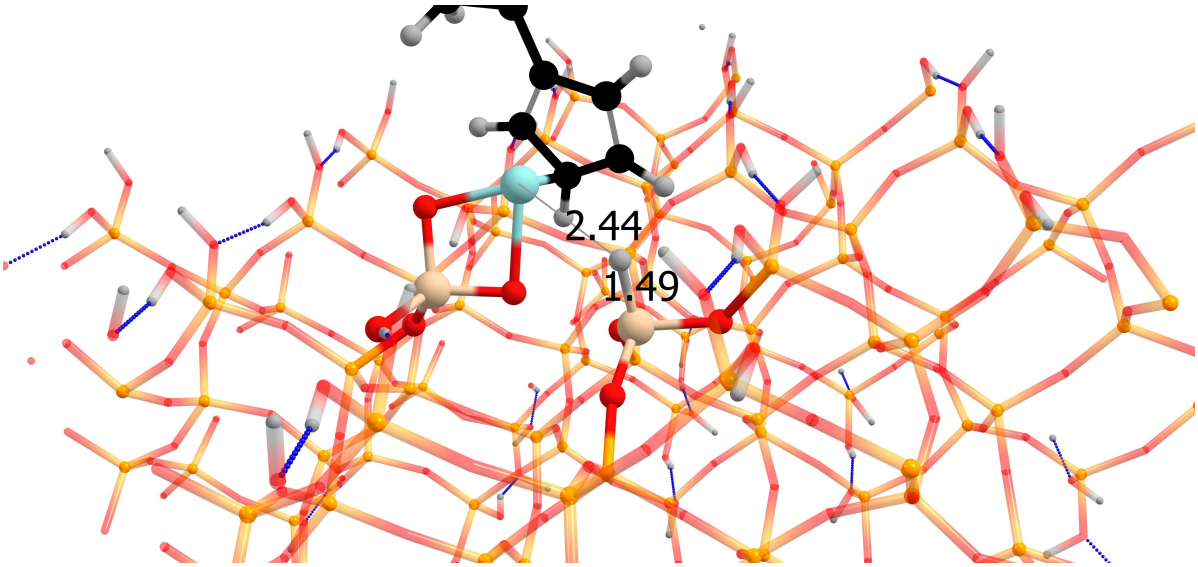

(b) TS2

Figure B.9: The optimized approximate transition states on a **cristobalite** silica surface. (a) the TS between the IS and IntS (b) the TS between the IntS and FS. The visual representation of the structure uses grey for hydrogen, black for carbon, red for oxygen, beige for silicon in the active site, orange for silicon in the surface, cyan for zirconium. The active site is highlighted by the use of larger spheres to represent the atoms. The Zr-H and Si-H distances are shown in Å. For visual clarity the front ^{Bu}Cp ring has been removed.

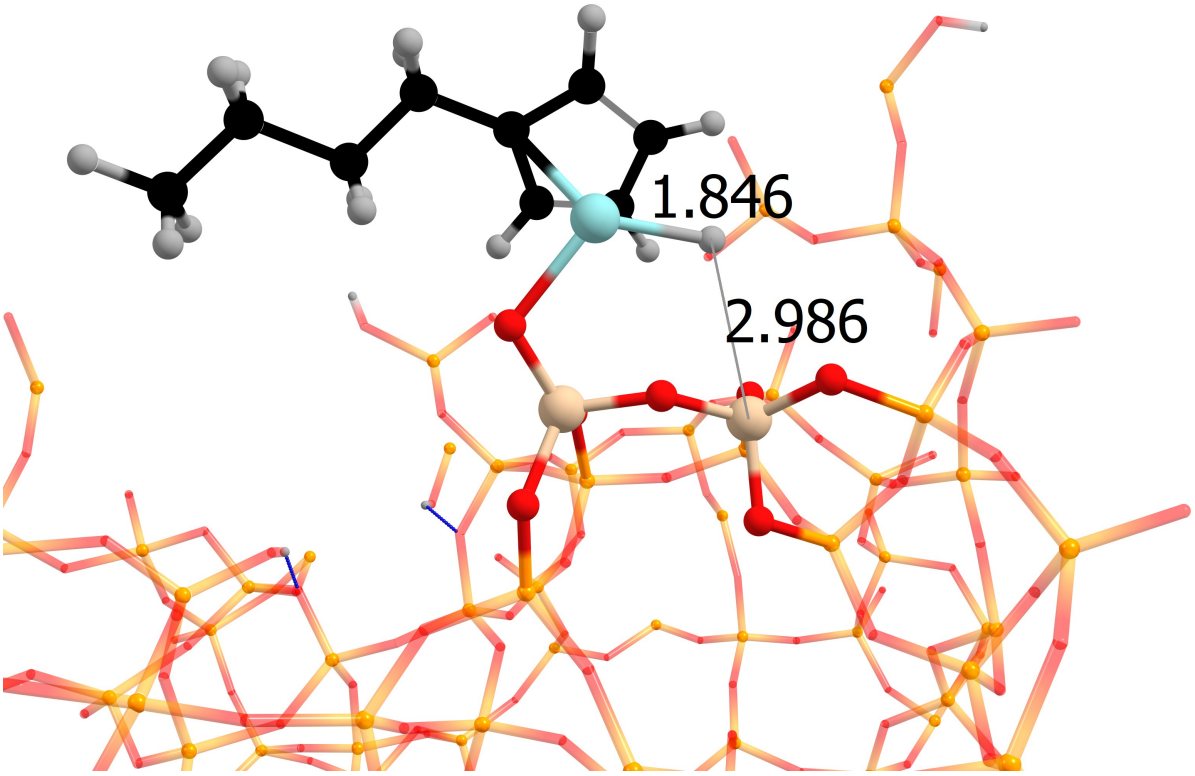

(a) TS1

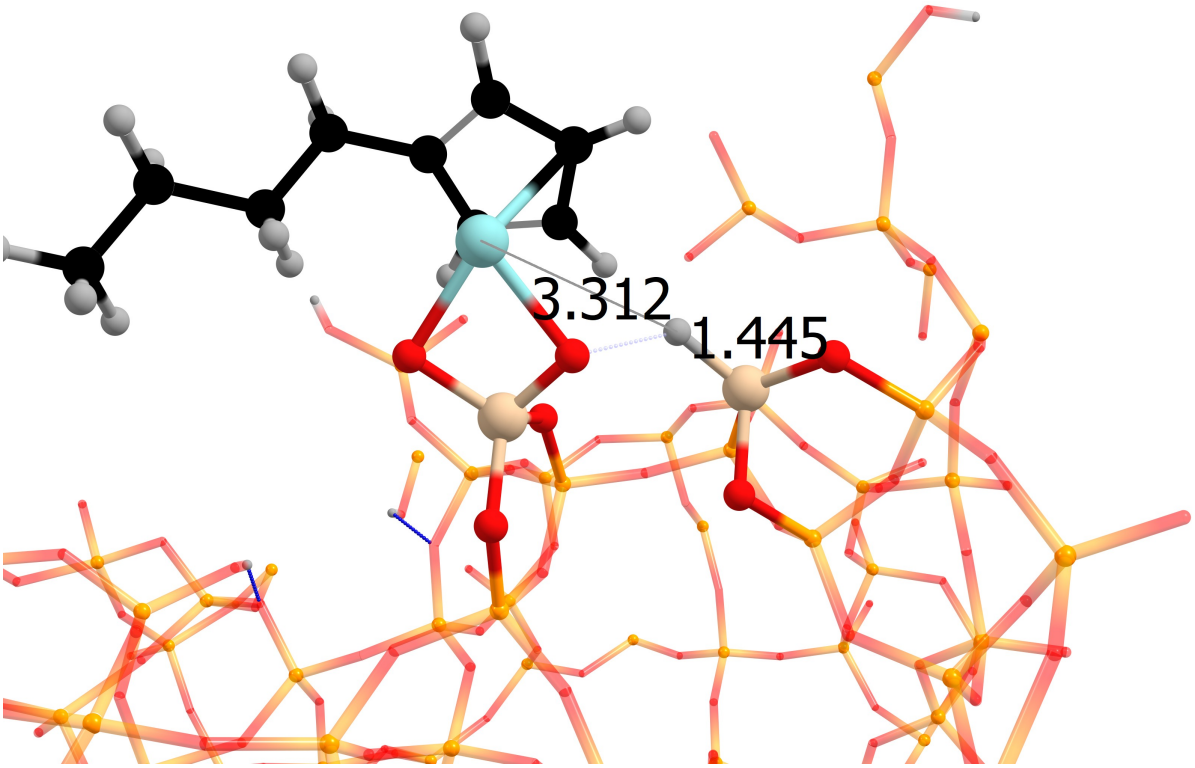

(b) TS2

Figure B.10: The optimized approximate transition states on a **minimum strain** amorphous silica surface. (a) the TS between the IS and IntS (b) the TS between the IntS and FS. The visual representation of the structure uses grey for hydrogen, black for carbon, red for oxygen, beige for silicon in the active site, orange for silicon in the surface, cyan for zirconium. The active site is highlighted by the use of larger spheres to represent the atoms. The Zr-H and Si-H distances are shown in Å. For visual clarity the front ^{Bu}Cp ring has been removed.

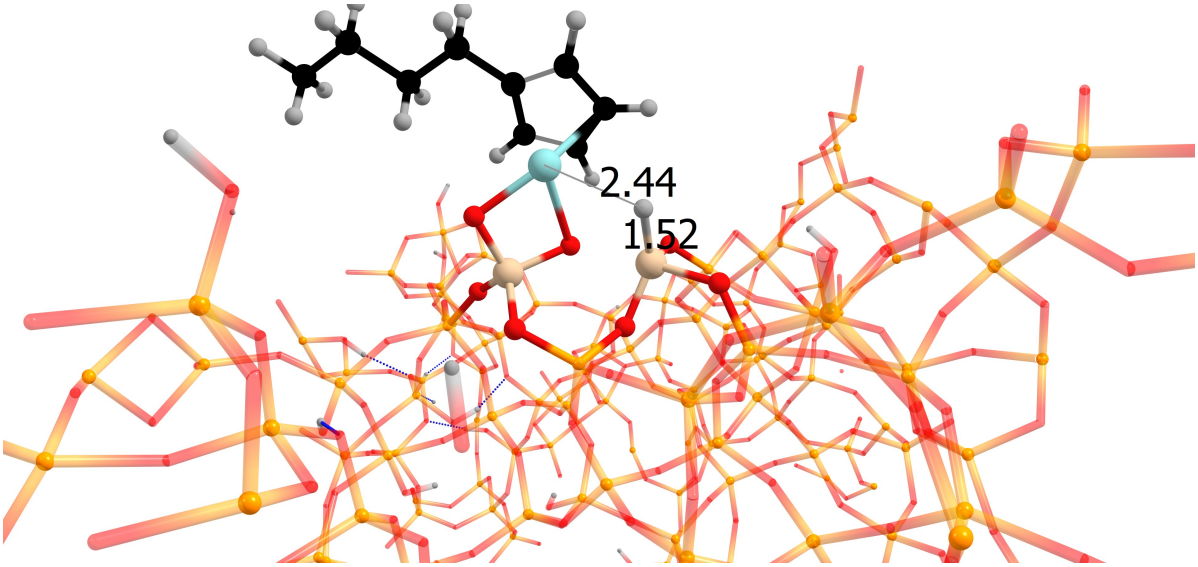

Figure B.11: The optimized approximate transition state of the second reaction barrier on an **average strain** amorphous silica surface. The visual representation of the structure uses grey for hydrogen, black for carbon, red for oxygen, beige for silicon in the active site, orange for silicon in the surface, cyan for zirconium. The active site is highlighted by the use of larger spheres to represent the atoms. The Zr-H and Si-H distances are shown in Å. For visual clarity the front ^{Bu}Cp ring has been removed.

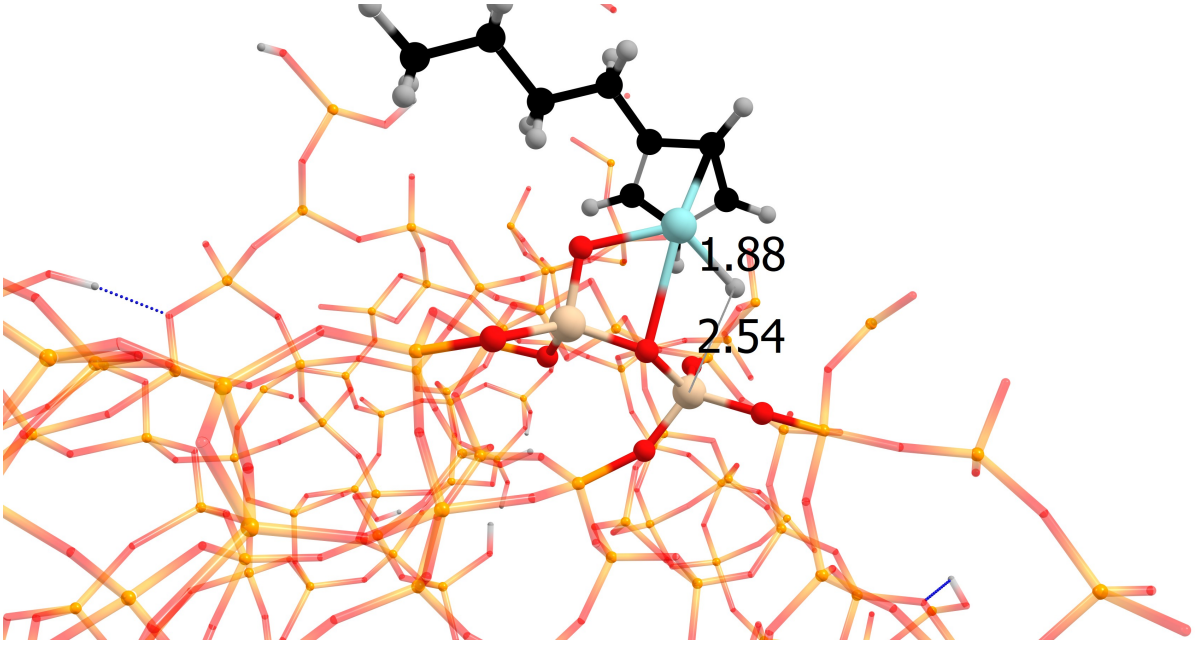

(a) TS1

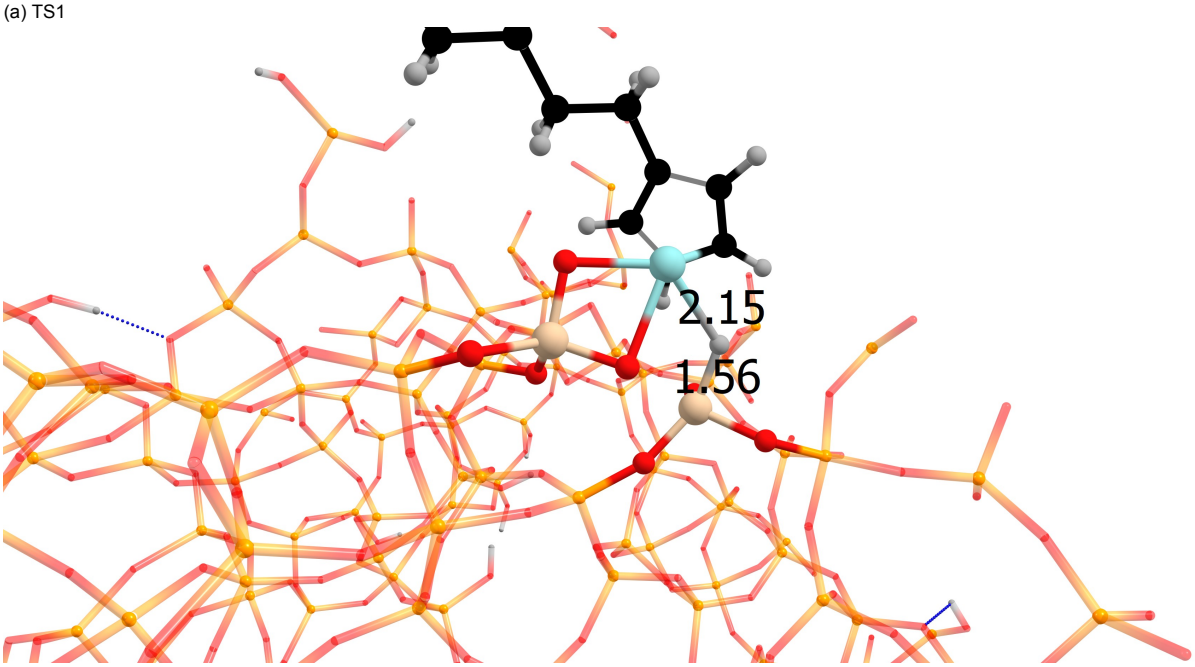

(b) TS2

Figure B.12: The optimized approximate transition states on a **maximum strain** amorphous silica surface. (a) the TS between the initial state and intermediate (b) the TS between the intermediate and final state. The visual representation of the structure uses grey for hydrogen, black for carbon, red for oxygen, beige for silicon in the active site, orange for silicon in the surface, cyan for zirconium. The active site is highlighted by the use of larger spheres to represent the atoms. The Zr-H and Si-H distances are shown in Å. For visual clarity the front ^{Bu}Cp ring has been removed.

B.3. Tables

Surface	E_a1 kJ/mol	k_1 s^{-1}	E_a2 kJ/mol	k_2 s^{-1}
Non-reconstructed	30	2.7E8	54	7.5E4
Reconstructed	36	3.5E7	13	8.8E10
β-cristobalite	96	4.6E-2	30	2.7E8
minium strain	17	2.2E10	107	1.1E-3
average strain	N/A	N/A	18	1.6E10
maximum strain	19	1.1E10	18	1.6E10

Table B.1: All reaction barrier energies with their respective rate constant. The number behind E_a show if it is the reaction barrier of the first or second reaction in the investigated mechanism.

C

Appendix: additional remarks

C.1. Acknowledgements

I would like to acknowledge my daily supervisor Dr. Kolganov and the Prof. Pidko of ISE for their invaluable support in this project. I would also like to thank Mas Klein for providing new amorphous silica surfaces. Finally I would also like to thank the rest of the ISE team including BEP students Nina and Joyce for their support and help in my project.

We thank SURF (www.surf.nl) for the support in using the National Supercomputer Snellius. Snellius was used to run all geometry optimizations, NEB calculations and vibrational analysis calculations.

The authors acknowledge the use of computational resources of the DelftBlue supercomputer, provided by Delft High Performance Computing Centre (https://www.tudelft.nl/dhpc).

C.2. Use of generative AI

Generative AI was used in the creation of the python programs/scripts to increase productivity. For example programs that format files, translate structures, submit jobs and manage naming conventions.

C.3. Data management

Generally speaking directories of jobs are saved with the name: 'calculation type_project code_iteration number'. Where the calculation types can be: NEB for a nudged elastic band calculation, GEO_OPT for a geometry optimization. The project code starts with "P[project_number]. The project numbers mean:

- 1: Non-reconstructed amorphous silica surface.
- 2: Reconstructed amorphous silica surface.
- 3: A variation of the reaction mechanism on a siloxane ring. (deprecated)
- 4: A variation of the reaction mechanism, that included parallel Si=O formation. (deprecated)
- 5: Cristobalite silica surface.
- 6: Minimum strain amorphous silica surface.
- 7: Average strain amorphous silica surface.
- 8: Maximum strain amorphous silica surface.

The project code continues with an optional indication of different initial or final structures on the surface/ with the reaction. An example can be seen with P1_I2, the I2 in this case means the second initial position. Then the states that are included in this calculation are given with ”S[state number(s)]”, where 1 is the initial state, 2 the intermediate and 3 the final state. The delimiter to combine the part of the project name is the underscore (_) as is done the same in the general naming structure. The iteration number is to differentiate similar calculations and is increased by one every new calculation as the name suggest. Sometimes extra abbreviations are added behind the total name or in between the iteration number: test to signify this calculation was at first a test, dep to signify deprecated meaning this calculation has something wrong with it(failed, mismatched structures, etc.).

C.3.1. VASP

Inside directories for NEB calculations can be directories with geometry optimizations and frequency analysis. Geometry optimization is again denoted by GEO_OPT, but instead of a project number ’Replica_[replica number]’ is added to show which replica is optimized. Frequency analysis is started with FREQ and is ended with an iteration number.

C.3.2. CP2K

For long term data storage the same logic applies as can be seen below using regular expressions.

```
Calculations
├── CP2K
│   └── P^[1-8]$
│       ├── ^GEO_OPT_P[1-8](_(I\d+)?(E\d+)?_S\d{1}_?.*_\d+)?_?.*$
│       └── ^NEB_P[1-8](_(I\d+)?(E\d+)?_S\d{1}_?.*_\d+)?_?.*$
│           └── ^GEO_OPT_dimer_P[1-8](_(I\d+)?(E\d+)?_S\d{1}_?.*_\d+)?_?.*$
│               └── ^VIB_P[1-8](_(I\d+)?(E\d+)?_S\d{1}_?.*_\d+)?_?.*$
└── VASP
    └── P^[1-8]$
        ├── ^GEO_OPT_P[1-8](_(I\d+)?(E\d+)?_S\d{1}_?.*_\d+)?_?.*$
        └── ^NEB_P[1-8](_(I\d+)?(E\d+)?_S\d{1}_?.*_\d+)?_?.*$
            ├── ^GEO_OPT_[Rr]eplica(_)?\d+$
            └── ^FREQ_analysis_\d+$
Code
├── python
└── bash
Templates
structures
Writing
├── Figures
│   ├── Made
│   └── Literature
└── Thesis
```